Title

Using dynamic mode decomposition to predict the dynamics of a two-time non-equilibrium Green's function

Authors

Yin, Jia
Chan, Yang-hao
da Jornada, Felipe H
et al.

Publication Date

2022-10-01

DOI

10.1016/j.jocs.2022.101843

Using Dynamic Mode Decomposition to Predict the Dynamics of a Two-time Non-equilibrium Green's function

Jia Yin[a,*], Yang-hao Chan[b], Felipe H. da Jornada[c], Diana Y. Qiu[d], Steven G. Louie[e,f], Chao Yang[a,*]

[a] *Applied Mathematics & Computational Research Division, Lawrence Berkeley National Laboratory, Berkeley, CA 94720, USA*
[b] *Institute of Atomic and Molecular Sciences, Academia Sinica, Taipei 10617, Taiwan*
[c] *Department of Materials Science and Engineering, Stanford University, Stanford, CA 94305, USA*
[d] *School of Engineering & Applied Science, Yale University, New Haven, CT 06520, USA*
[e] *Department of Physics, University of California at Berkeley, Berkeley, CA 94720, USA*
[f] *Materials Sciences Division, Lawrence Berkeley National Laboratory, Berkeley, CA 94720, USA*

Abstract

Computing the numerical solution of the Kadanoff-Baym equations, a set of nonlinear integral differential equations satisfied by the two-time Green's functions derived from many-body perturbation theory for a quantum many-body system away from equilibrium, is a challenging task. Recently, we have successfully applied dynamic mode decomposition (DMD) to construct a data driven reduced order model that can be used to extrapolate the time-diagonal of a two-time Green's function from numerical solution of the KBE within a small time window. In this paper, we extend the previous work and use DMD to predict off-diagonal elements of the two-time Green's function. We partition the two-time Green's function into a number of one-time functions along the diagonal and subdiagonls of the two-time window as well as in horizontal and vertical directions. We use DMD to construct separate reduced order models to predict the dynamics of these one-time functions in a two-step procedure. We extrapolate along diagonal and several subdiagonals within a subdiagonal band of a two-time window in the first step. In the second step, we use DMD to extrapolate the Green's function outside of the sub-diagonal band. We demonstrate the efficiency and accuracy of this approach by applying it to a two-band Hubbard model problem.

Keywords: Kadanoff-Baym equation, two-time Green's function, dynamic mode decomposition, non-equilibrium quantum many-body dynamics

1. Introduction

Simulating a quantum many-body system away from equilibrium is a challenging task. Although time-dependent physical observables can be computed from the solution of a time-dependent Schrödinger equation with a time-dependent Hamiltonian, such a brute-force approach is limited to small systems defined in a small dimensional Hilbert space. For many physical properties of interest, a more practical approach is to focus on the Green's function, $G(t, t')$, which is a two-point correlator of the creation and annhilation field

*Corresponding author: Tel.: +1-925-285-2235 (Jia Yin), +1-510-486-6424 (Chao Yang); fax: +1-510-486-5812 (Chao Yang)
Email addresses: jiayin@lbl.gov (Jia Yin), sglouie@berkeley.edu (Steven G. Louie), cyang@lbl.gov (Chao Yang)

operators defined on the Keldysh contour [1, 2, 3, 4]. Unlike the equilibrium Green's function, which depends on $t - t'$ and hence is a one time function, the non-equilibrium Green's function depends on both t and t'. The equation of motion satisfied by the two-time non-equilibrium Green's function is a set of nonlinear integro-differential equations of the form

$$\left[i\frac{d}{dt} - H(t)\right] G(t,t') = \delta(t,t') + \int_C \Sigma(t,\bar{t})G(\bar{t},t')d\bar{t}, \tag{1.1}$$

where $H(t)$ is a single-particle Hamiltonian, $\Sigma(t,t')$ is a self-energy that accounts for the many-body interactions and generally can depend on the Green's function G. Equation (1.1) and its accompanying adjoint equation which describes the propagation of $G(t,t')$ along the t' direction are often referred to as the Kadanoff-Baym equations (KBE) [2].

Evolving the Green's function numerically on a two-time grid is highly non-trivial. A commonly used method to solve the KBE system (1.1) is a nonlinear time evolution scheme based on an implicit Runge-Kutta method and a fixed point iteration [5, 6]. Other numerical methods for solving this type of nonlinear integral differential equations have been proposed in [7, 8, 9, 10, 11, 12, 13, 14, 15] and the references therein. In all these methods, the presence of the integral term in the KBEs makes both the memory requirement and computational cost high if the long-time behavior of a physical observable is to be examined [16].

One possible way to reduce the computational cost is to use model order reduction techniques to simplify the time evolution of the Green's function while retaining the key features of the dynamics. These techniques construct models with fewer degrees of freedom to approximate the original system. The use of a reduced order model can lead to a significant reduction in computational cost without sacrificing much accuracy. Among these techniques, the dynamic mode decomposition (DMD) technique, originally introduced by Schmid [17], is a promising approach. DMD has been successfully applied to various applications in fluid dynamics [18, 19, 20, 21], video processing [22, 23] and epidemiology [24]. However, to the best of our knowledge, DMD has not been widely used for simulating the dynamics of a quantum many-body system. We will show in this paper that DMD can be used to approximate the two-time nonequilibrium Green's function without solving the KBEs (1.1) on a large two-time grid.

In our previous work [25], we applied DMD to predict the time diagonal of the Green's function, i.e, $\rho(t) = G(t,t)$, for large t, from a linear reduced order model constructed from the numerical solution of the KBE within a small two-time window. Even though the two-time dynamics satisfied by $G(t,t')$ can be nonlinear, we observed that the one-time dynamics satisfied by $\rho(t)$, which cannot be easily written down analytically, can be well approximated by a linear model.

In this paper, we extend the technique developed in [25] to predict the entire two-time Green's function $G(t,t')$ from the numerical solution of the KBE from a small time window. Our basic strategy is to divide the two-time $G(t,t')$ into a number of one-time functions and construct a DMD-based reduced order model for each one of them. We examine a few different ways to perform such divisions and approximations. In one approach, we treat $G(t,t')$ for a fixed $t - t'$ as a one-time function that satisfies a one-time dynamical system. The prediction of such time-subdiagonal of $G(t,t')$ is a natural extension of the prediction of the

time diagonal of $G(t,t')$ we developed in the previous work. After the prediction of several time-subdiagonals of $G(t,t')$ have been made, we can then use either the computed or extrapolated $G(t,t')$ for a fixed t' to construct a reduce order model to predict the values of $G(t,t')$ for large t, i.e. away from the time-diagonal. This two-step procedure is compared with an alternative approach in which we first fix t' and extrapolate along the t direction, and then fix t and extrapolate along the t' direction. The DMD method employed in both of these two approaches provides a momentum-temporal decomposition of several one time functions. Numerical examples are presented to demonstrate the effectiveness of the DMD extrapolation for a simple Hubbard model driven by an external field with different intensity levels. Yet another alternative we consider in this paper is a decomposition that fixes the k-point (i.e., a momentum grid point) and treats one of the time variable as a spatial variable within a selected time window. The reduced order model constructed in this scheme allows us to extrapolate the values of $G(t,t')$ within a two-time sub-window for a specific k-point. We show, by numerical examples, that this approach can sometimes be more effective than a momentum-temporal decomposition.

The rest of the paper is organized as follows. In Section 2, we review the principal ideas and procedures of applying DMD. The implementation of DMD for the two-time Green's function is discussed in Section 3. In Section 4, we demonstrate the effectiveness of the proposed DMD schemes by numerical examples.

2. Dynamic mode decomposition

In this section, we provide an overview of the dynamic mode decomposition (DMD) method [17, 26] to be used in the next section to predict values of the two-time Green's function $G(t,t')$ for large t and t' from the numerical solution of the KBE within a small two-time window. We will also examine a variant of DMD called high order DMD (HODMD), which was originally developed by Clainche and Vega [27] to yield more accurate prediction from spatially undersampled data.

DMD is a data-driven dimension reduction technique used to construct a low dimensional linear dynamical model that can be used to predict observables of a nonlinear dynamical system with a large number of degrees of freedom [17, 19, 26, 28]. The linear model can be characterized by a number of spatial and temporal modes that can be obtained from the eigenvalues and eigenvectors of a linear operator.

To describe the basic idea of DMD, consider a nonlinear dynamical system defined by the ordinary differential equation

$$\frac{d\mathbf{x}(t)}{dt} = \mathbf{f}(\mathbf{x}(t), t), \quad t \geq 0, \tag{2.1}$$

where $\mathbf{x}(t) \in \mathbb{C}^n$ is a time-dependent state variable, and $\mathbf{f} : \mathbb{C}^n \otimes \mathbb{R}^+ \to \mathbb{C}^n$ is a nonlinear function of $\mathbf{x}$ and time t.

If we were to approximate (2.1) by a linear model

$$\frac{d\mathbf{x}(t)}{dt} = \mathbf{A}\mathbf{x}(t), \tag{2.2}$$

what is the best choice of the linear operator $\mathbf{A}$? This question is important for problems in which distinct features such as certain oscillation frequencies and amplitude decay rates are of interest even though the overall dynamics cannot be easily described by a linear model. For problems that have an explicit analytical expression of $\mathbf{f}(\mathbf{x}(t), t)$, it may be possible to linearize $\mathbf{f}(\mathbf{x}(t), t)$ and derive $\mathbf{A}$ explicitly. This linearization process essentially amounts to a linear response analysis. However, when the analytical form of $\mathbf{f}(\mathbf{x}(t), t)$ is unknown, performing such an analysis is difficult, if not impossible.

The linearization produced by DMD is based the Koopman operator theory [29, 30, 31], which is developed to characterize the evolution of a scalar obervable function of $\mathbf{x}(t)$, denoted by $g(\mathbf{x}(t))$, to $g(\mathbf{x}(t + \Delta t))$ with $\Delta t > 0$, i.e.

$$g(\mathbf{x}(t + \Delta t)) = \mathcal{K}_{\Delta t} g(\mathbf{x}(t)).$$

In the limit of $\Delta t \to 0$, the Koopman operator defines a linear dynamical system

$$\frac{dg(\mathbf{x}(t))}{dt} = \mathcal{K} g(\mathbf{x}(t)). \tag{2.3}$$

Because the Koopman operator $\mathcal{K}$ is a linear operator that maps from a function space to another function space, it has infinite number of eigenvalues λ_j and eigenfunctions $\varphi_j(\mathbf{x})$, $j = 1, 2, ..., \infty$.

If the observable functions of interest can be well approximated by an invariant subspace of $\mathcal{K}$ defined by a finite subset of eigenvalues and eigenvectors, then it is possible to construct a finite dimensional operator (matrix) approximation to $\mathcal{K}$.

To be specific, if $g_1(\mathbf{x})$, $g_2(\mathbf{x})$,...,$g_n(\mathbf{x})$ are n observable functions that can be expressed as

$$\begin{bmatrix} g_1(\mathbf{x}) \\ g_2(\mathbf{x}) \\ \vdots \\ g_n(\mathbf{x}) \end{bmatrix} = \begin{bmatrix} v_1 & v_2 & \cdots & v_k \end{bmatrix} \begin{bmatrix} \varphi_1(\mathbf{x}) \\ \varphi_2(\mathbf{x}) \\ \vdots \\ \varphi_k(\mathbf{x}), \end{bmatrix}$$

for some vectors $v_1, v_2, ..., v_k \in \mathbb{C}^n$, which contain the expansion coefficients, then $\mathcal{K}$ can be approximated by a $k \times k$ matrix $\mathbf{A}$.

To construct such an approximation for observable functions that are chosen to be the components of $\mathbf{x}(t)$ defined in (2.1), we take snapshots of $\mathbf{x}(t)$ at $t_j = (j-1)\Delta t$, i.e., $\mathbf{x}_j = \mathbf{x}(t_j)$, for $j = 1, ..., m$, and use them to build two matrices $\mathbf{X}_1$ and $\mathbf{X}_2$ of the form

$$\mathbf{X}_1 = (\mathbf{x}_1\, \mathbf{x}_2\, \cdots\, \mathbf{x}_{m-1}) \quad \text{and} \quad \mathbf{X}_2 = (\mathbf{x}_2\, \mathbf{x}_3\, \cdots\, \mathbf{x}_m)\,. \tag{2.4}$$

The finite dimensional approximation to the Koopman operator can then be obtained by solving the following linear least squares problem

$$\min_{\mathbf{A}} \|\mathbf{A}\mathbf{X}_1 - \mathbf{X}_2\|_F^2. \tag{2.5}$$

The solution to (2.5) is

$$\mathbf{A} = \mathbf{X}_2 \mathbf{X}_1^{\dagger}, \tag{2.6}$$

where $\mathbf{X}_1^\dagger$ is the Moore-Penrose pseudoinverse of $\mathbf{X}_1$ that can be computed from the singular value decomposition (SVD) [32] of $\mathbf{X}_1$. If the nonzero singular values of $\mathbf{X}_1$, σ_j, $j = 1, 2, ..., m$, decrease rapidly with respect to j, which indicates that the numerical rank, denoted by r, of $\mathbf{X}_1$ is much smaller than m and n, we can use a truncated SVD of $\mathbf{X}_1$ in the form of $\mathbf{X}_1 = \widetilde{\mathbf{U}}\widetilde{\mathbf{\Sigma}}\widetilde{\mathbf{V}}^T$, where the $r \times r$ diagonal matrix $\widetilde{\mathbf{\Sigma}}$ contains the leading r dominant singular values of $\mathbf{X}_1$, and $\widetilde{\mathbf{U}}$ and $\widetilde{\mathbf{V}}$ contain the corresponding right and left singular vectors, to obtain an approximation of $\mathbf{A}$ as

$$\mathbf{A} \approx \mathbf{X}_2\widetilde{\mathbf{V}}\widetilde{\mathbf{\Sigma}}^{-1}\widetilde{\mathbf{U}}^*, \tag{2.7}$$

We can now fully characterize the approximated reduced order linear dynamical system model by diagonalizing the projected Koopman operator $\widetilde{\mathbf{A}} = \widetilde{\mathbf{U}}^*\mathbf{A}\widetilde{\mathbf{U}} = \widetilde{\mathbf{U}}\mathbf{X}_2\widetilde{\mathbf{V}}\widetilde{\mathbf{\Sigma}}^{-1}$. Let

$$\widetilde{\mathbf{A}}\mathbf{W} = \mathbf{W}\mathbf{\Lambda} \tag{2.8}$$

be the eigendecomposition of $\widetilde{\mathbf{A}}$, where $\mathbf{\Lambda} = \mathrm{diag}(\lambda_1, ..., \lambda_r)$ is composed of the eigenvalues of $\widetilde{\mathbf{A}}$, and the columns of $\mathbf{W}$ are the corresponding eigenvectors. The matrix

$$\mathbf{\Phi} = \mathbf{X}_2\widetilde{\mathbf{V}}\widetilde{\mathbf{\Sigma}}^{-1}\mathbf{W} \tag{2.9}$$

contains the so called DMD modes. If ϕ_ℓ is the ℓth column of $\mathbf{\Phi}$, the DMD approximation to $\mathbf{x}$ can be by represented by

$$\mathbf{x}(t) \approx \sum_{\ell=1}^{r} \phi_\ell \exp(i\omega_\ell^{\mathrm{DMD}} t) b_\ell = \mathbf{\Phi}\exp(\mathbf{\Omega}t)\mathbf{b}. \tag{2.10}$$

where $\omega_\ell^{\mathrm{DMD}} = -i\frac{\ln\lambda_\ell}{\Delta t}$, $\ell = 1, ..., r$, $\mathbf{\Omega} = \frac{\ln\mathbf{\Lambda}}{\Delta t} = \mathrm{diag}(i\omega_1^{\mathrm{DMD}}, ..., i\omega_r^{\mathrm{DMD}})$, and the amplitude vector $\mathbf{b} := [b_1, ..., b_r]^T$ is taken either as the projection of the initial value $\mathbf{x}_1$ onto the DMD modes, i.e.,

$$\mathbf{b} = \mathbf{\Phi}^\dagger\mathbf{x}_1, \tag{2.11}$$

or as the least squares fit of (2.10) on the sampled trajectories, i.e.,

$$\mathbf{b} = \arg\min_{\tilde{\mathbf{b}}\in\mathbb{C}^n} \sum_{j=1}^{m} \|\mathbf{\Phi}\exp(\mathbf{\Omega}t_j)\tilde{\mathbf{b}} - \mathbf{x}_j\|^2, \tag{2.12}$$

where $\|\cdot\|$ denotes the standard Euclidean norm of a vector. For more details on the numerical procedure, we refer readers to references [17, 26, 28, 25].

The major computational cost of DMD computation is in the SVD of $\mathbf{X}_1$, which is $O(\min(m^2n, mn^2))$. The memory cost is $O(mn)$.

As pointed out in [28, 33], the success of the DMD approximation to the Koopman operator depends crucially on the choice of observables. When the observables are chosen to be discretized components of $\mathbf{x}$, a limited resolution in the discretization may lead to a poor DMD approximation to the Koopman operator as shown in [25]. In particular, the number of DMD modes r, which can be extracted from the data, may be too small to represent the true dynamics of $\mathbf{x}(t)$. To overcome this difficulty, we choose to use the higher order

DMD (HODMD) method, which was derived from the time-delay embedding theory in [34, 35, 36, 37], to construct a better approximation to the Koopman operator in (2.3). For more details about the time-delay embedding theory and its relation to HODMD, we refer readers to [25] and [27].

In HODMD [27], each column of $\mathbf{X}_1$ and $\mathbf{X}_2$ consists of d consecutive snapshots. When the time step size between two adjacent columns is a constant Δt, the same snapshot may be used in several adjacent columns. This construction increases the leading dimension of the data matrices by a factor of d. Consequently, the cost of computing the HODMD modes is also higher. Furthermore, when Δt is small, the columns can become more linearly dependent. To reduce the computational cost and column linear dependency of the data matrices, we can increase the temporal distance between the augmented snapshots to make sure there is no overlapping between two columns of $\mathbf{X}_1$ and $\mathbf{X}_2$. Specifically, we can define the data matrices $\widetilde{\mathbf{X}}_1$ and $\widetilde{\mathbf{X}}_2$ as

$$\widetilde{\mathbf{X}}_1 = \begin{bmatrix} \mathbf{x}_1 & \mathbf{x}_{d+1} & \cdots & \mathbf{x}_{(p-2)d+1} \\ \mathbf{x}_2 & \mathbf{x}_{d+2} & \cdots & \mathbf{x}_{(p-2)d+2} \\ \vdots & \vdots & \vdots & \vdots \\ \mathbf{x}_d & \mathbf{x}_{2d} & \cdots & \mathbf{x}_{(p-1)d} \end{bmatrix}, \quad \widetilde{\mathbf{X}}_2 = \begin{bmatrix} \mathbf{x}_{d+1} & \mathbf{x}_{2d+1} & \cdots & \mathbf{x}_{(p-1)d+1} \\ \mathbf{x}_{d+2} & \mathbf{x}_{2d+2} & \cdots & \mathbf{x}_{(p-1)d+2} \\ \vdots & \vdots & \vdots & \vdots \\ \mathbf{x}_{2d} & \mathbf{x}_{3d} & \cdots & \mathbf{x}_{pd} \end{bmatrix}, \tag{2.13}$$

where $p = \text{floor}(m/d)$. We denote this choice of data matrices as HODMD[d].

Once $\widetilde{\mathbf{X}}_1$ and $\widetilde{\mathbf{X}}_2$ are prepared according to (2.13) in HODMD[d], we follow the same procedure used in DMD to compute the HODMD modes. The only difference is that the time step between two adjacent columns becomes $d \times \Delta t$ instead of Δt. As each column of $\widetilde{\mathbf{X}}_1$ consists of d consecutive snapshots, each spatial HODMD mode is a vector of length nd. Therefore, in the reconstruction and extrapolation of $\mathbf{x}(t)$ by (2.10), we only take the first n elements of each spatial HODMD mode as ϕ_ℓ, $\ell = 1, ..., r$.

We remark here that we use HODMD instead of DMD in all the examples presented in this paper in order to compensate for the possible lack of spatial/momentum resolution. But for simplicity, in the next section, we use DMD to demonstrate the main features of this type of approach. As mentioned above, the basic algorithmic steps performed in HODMD are the same as those in DMD, except that the data matrices used in HODMD are augmented as shown in (2.13), and we only take the first n_k rows of the extrapolated results as the approximation to the desired Green's function.

3. DMD for the two-time Green's function

In this section, we propose two ways to use DMD to extrapolate the entire two-time Green's function from the numerical solutions of the KBE in a small time window. In the first approach to be presented in section 3.1, we extrapolate along one fixed time direction, and refer this scheme as a fixed timeline (FT) DMD extrapolation. In the second approach to be presented in section 3.2, we extrapolate on a two-time grid for each fixed k-point, and refer to this scheme as a fixed k-point (FK) DMD extrapolation.

3.1. DMD of $G(t,t')$ for a fixed $t-t'$ or t'

In our previous work [25], we applied the DMD technique to analyze and extrapolate the time-diagonal of the two-time Green's function $G(t,t')$ from the numerical solution of the KBEs (1.1) within a small time window.

To be specific, we solved the KBE within the time window $[0,t_m]\times[0,t_m]$ for a sufficiently small time step Δt and a small integer m. The time-diagonal of the Green's function $\rho(k_s;t_j) := G(k_s;(j-1)\Delta t,(j-1)\Delta t)$, with $s=1,\ ...,\ n_k,\ j=1,\ ...,\ m$ were used to construct a snapshot matrix $\mathbf{X}$ as

$$\mathbf{X} = [\rho(\mathbf{k},t_1),\ \rho(\mathbf{k},t_2),\ ...,\ \rho(\mathbf{k},t_m)]\,, \tag{3.1}$$

where $\mathbf{k} := (k_1,\ ...,\ k_{n_k})^T$ denotes the uniformly sampled k-points in the Brillouin zone of the momentum space, and each snapshot $\rho(\mathbf{k},t_j)$ is defined as

$$\rho(\mathbf{k},t_j) := (\rho(k_1,t_j),\ \rho(k_2,t_j),\ ...,\ \rho(k_{n_k},t_j))^T\,,\quad j=1,...,m. \tag{3.2}$$

We have shown that, for a two-band Hubbard model driven by an external field, DMD can successfully predict the long-time dynamics of ρ from $\mathbf{X}$ when the intensity of the driving field is relatively small. The numerical experiments presented in [25] also show that for high intensity driving field, HODMD produces more accurate prediction of $\rho(\mathbf{k},t)$ for large t values.

The success of DMD and HODMD is partly due to the fact that the time diagonal of $G(t,t')$ is well behaved, i.e., the real and imaginary parts of this function are smooth, and they exhibit clear oscillation and decay properties.

It has been observed that the smoothness property of $G(t,t')$ also holds for $t'-t=\tau$, where $\tau>0$ is fixed. As an example, Figure 3.1 shows $G(t+0.9,t)$, i.e., $\tau=0.9$, for the same two-band Hubbard model examined in [25]. Therefore, we can, in principle, use the same DMD techniques we developed for predicting the time diagonal of G to predict the time subdiagonals of G.

However, to generate a snapshot matrix $\mathbf{X}$ for the j-th subdiagonal of G with m snapshots, we need to increase the size of the sampled time window in which the KBE is solved numerically from $[0,t_m]\times[0,t_m]$ to $[0,t_{m+j}]\times[0,t_{m+j}]$. The $n_k\times m$ snapshot matrix $\mathbf{X}$ for the j-th subdiagonal $G(\mathbf{k};t+j\Delta t,t)$ is therefore given by

$$\mathbf{X} = [G(\mathbf{k},t_{1+j},t_1),\ G(\mathbf{k},t_{2+j},t_2),\ ...,\ G(\mathbf{k},t_{m+j},t_m)]\,. \tag{3.3}$$

In general, if the diagonal and $\ell-1$ subdiagonals of $G(t,t')$ are to be analyzed and extrapolated, we need to solve the KBE within the time window of $[0,t_{m+\ell-1}]\times[0,t_{m+\ell-1}]$. Figure 3.2 gives a schematic depiction of the time window in which the KBE is solved. The shaded region contains the snapshots to be used for DMD analysis. The extrapolated subdiagonal elements of $G(t,t')$ are contained in the parallelogram denoted by the blue dashed lines. Note that, within the time window $[0,t_{m+\ell-1}]\times[0,t_{m+\ell-1}]$, we can use more snapshots to perform DMD for the subdiagonals closer to the diagonal.

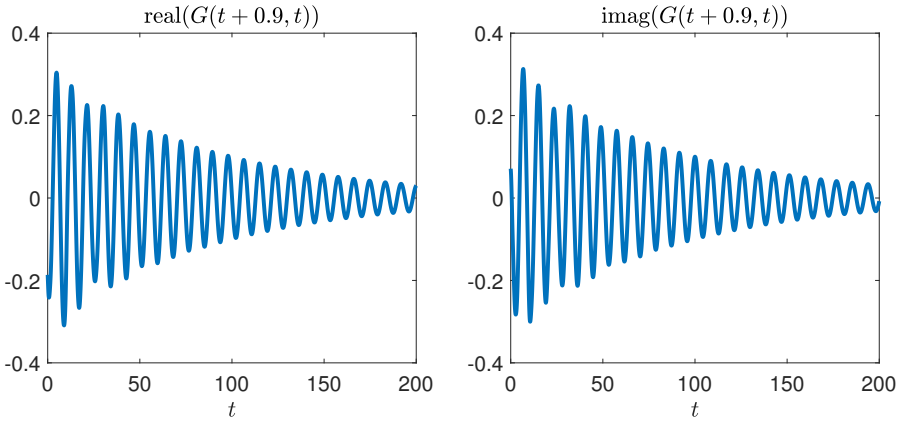

Figure 3.1: The subdiagonal $G(t+0.9,t)$ for the two-band Hubbard model with the intensity of the external field $I = 0.5$ at $k = 0$.

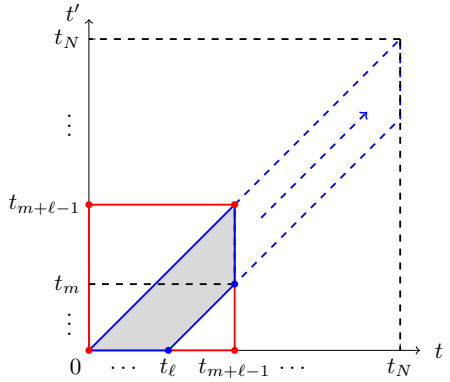

Figure 3.2: To use DMD to predict $G(t,t')$ along the time-diagonal and $\ell-1$ time-subdiagonals (contained in the parallelogram outlined by the blue dashed lines), we need to solve the KBE numerically within the time window $[0,t_{m+\ell-1}]\times[0,t_{m+\ell-1}]$ (drawn in red). The snapshot matrices are constructed by extracting subdiagonals of $G(t,t')$ within the shaded parallelogram contained in the solid blue lines.

125 To obtain values of $G(t,t')$ for t and t' that are outside of the subdiagonal band, we rely on another observation that shows $G(t,t')$ is typically smooth with respect to t for a fixed t' and vice versa. For example, In Figure 3.3, we plot the real and imaginary parts of $G(t,t')$ at $t' = 50$. Both curves are smooth with clear oscillation frequencies and amplitude envelops.

Therefore, we can utilize values in the subdiagonal band to extrapolate those that are outside the band. To be specific, for a fixed $t' = t_j$, the $n_k \times \ell$ data matrix $\mathbf{X}$ to be used in DMD is constructed as

$$\mathbf{X} = [G(\mathbf{k},t_j,t_j),\ G(\mathbf{k},t_{j+1},t_j),\ ...,\ G(\mathbf{k},t_{j+\ell-1},t_j)]\,. \tag{3.4}$$

If $j \le m$, then from Figure 3.2, these data can be taken from the numerical solution to KBE. Otherwise,

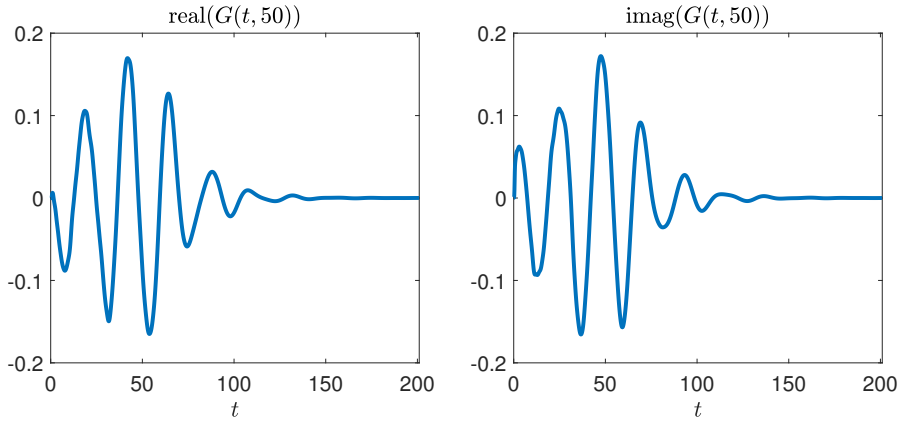

Figure 3.3: $G(t, 50)$ for the two-band Hubbard model with the intensity of the external field $I = 0.5$ at $k = 0$.

they are approximated by subdiagonal extrapolations produced in the previous steps.

What we have described is one possible way to apply DMD to predict $G(t, t')$ for large t and t' values from the numerical solution of the KBE within a small time window. We first apply DMD to the data matrices (3.3) to extrapolate the values in the subdiagonal band $G(t + j\Delta t, t)$ with $j = 0, 1, ..., \ell - 1$. Subsequently, we use the solutions in the subdiagonal band to predict the values of $G(t, t')$ outside the subdiagonal band. As in each step, one time direction is always fixed ($t - t'$ for the first step, and t' for the second step), we call this method fixed timeline (FT) DMD extrapolation.

3.2. DMD of $G(t, t')$ for a fixed k-point

DMD is traditionally used to perform a spatial-temporal decomposition of one-time nonlinear dynamics.

In the previous section, we took the more traditional approach by fixing either $t - t'$ or t' and performing a DMD in the two dimensions defined by momentum (k) and time (t) for a fixed $t - t'$ or t'.

However, the DMD algorithm itself is agnostic to the physical interpretation of the variables and the data. All it requires are a few slices of data that are related and vary smoothly from one slice to another. These data slices can be combined and viewed as a data matrix on which a truncated singular value decomposition can be performed. Once the DMD modes and frequencies are computed, they can be assembled to construct a reduced order model for predicting additional data slices.

In this section, we take an alternative approach in using DMD to analyze and predict the two-time Green's function. Instead of fixing t' or $t - t'$, we fix the k-point, and apply DMD directly to $G(t, t')$.

The simplest scheme is to take the numerical solution of the KBE within the time window $[0, t_{m_1}] \times [0, t_{m_2}]$ for a fixed k-point as the snapshot matrix, and perform DMD to extrapolate and predict the values of $G(t, t')$ for $0 \leq t' \leq t_{m_2}$ and $t > t_{m_1}$ as the first step. This procedure is illustrated in Figure 3.4. Then, in the second step, the computed or extrapolated values of $G(t, t')$ within $[0, t_N] \times [0, t_{m_2}]$ are used to predict values of $G(t, t')$ for $t' > t_{m_2}$.

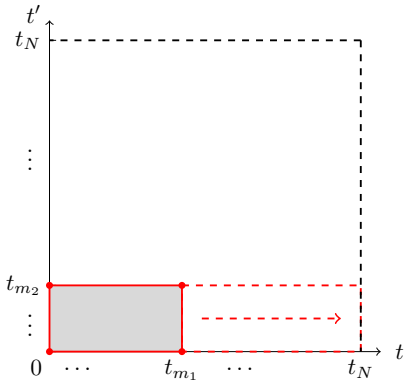

Figure 3.4: Illustration of the extrapolation of $G(t,t')$ along the t direction by applying DMD to the sampled window $[0,t_{m_1}]\times[0,t_{m_2}]$ given by the shaded rectangle.

Note that the KBE is typically solved for $t' \leq t$. The values of $G(t,t')$ in the upper triangular part of the time window $0 \leq t \leq t_{m_1}$ and $t' > t$ can be obtained from symmetry properties of G. However, because the amplitude envelop of $G(t,t')$ is typically different for $t < t'$ and $t \geq t'$ (for a fixed t') (see Figure 3.3), using the values of $G(t,t')$ for $t \leq t'$ to predict $G(t,t')$ for $t > t'$ may not work well as we will show in Section 4.

An alternative scheme, which only requires taking snapshots within the lower triangular time window $t' \leq t$ for a fixed k-point is to sample along the diagonal and subdiagonals of $G(t,t')$, i.e., we can construct the snapshot matrix as

$$\mathbf{X} = \begin{bmatrix} G(t_1,t_1) & G(t_2,t_2) & \cdots & G(t_m,t_m) \\ G(t_2,t_1) & G(t_3,t_2) & \cdots & G(t_{m+1},t_m) \\ \vdots & \vdots & \cdots & \vdots \\ G(t_m,t_1) & G(t_{m+1},t_2) & \cdots & G(t_{2m-1},t_m) \end{bmatrix}. \tag{3.5}$$

The matrix elements contained in (3.5) correspond to values of $G(t,t')$ evaluated within the parallelogram outlined in blue and marked as area (I) in Figure 3.5. Each column of $\mathbf{X}$ corresponds to each row of the $G(t,t')$ within that parallelogram. In general, the number of rows in $\mathbf{X}$ can be different from the number of columns, i.e., we can sample along the t' direction up to $t' = t_{m_1} = (m_1-1)\Delta t$, and along the t direction up to $t = t_{m_2}$ for $t' = 0$ and $t = t_{m_1+m_2-1}$ for $t' = t_{m_1}$ (starting from $t = t_{m_1}$) as shown in Figure 3.5.

Once we perform a DMD on this snapshot matrix, we can extrapolate along the diagonal and subdiagonals of $G(t,t')$ first, as indicated by the dashed arrow in the left panel of Figure 3.5.

To predict values of $G(t,t')$ outside of the subdiagonal bands in the second step, we can sample within a parallelogram time window outlined in red and marked by area (II) in the right panel of Figure 3.5 to

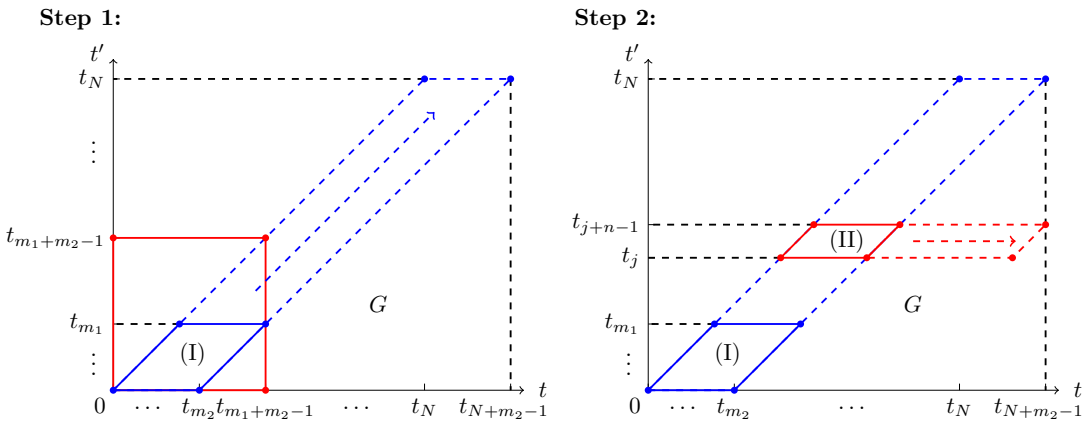

Figure 3.5: Illustration of the two-step DMD for the Green's function $G(t,t')$ at a fixed k-point.

construct a snapshot matrix of the form

$$\mathbf{X} = \begin{bmatrix} G(t_j,t_j) & G(t_{j+1},t_j) & \cdots & G(t_{j+m_2-1},t_j) \\ G(t_{j+1},t_{j+1}) & G(t_{j+2},t_{j+1}) & \cdots & G(t_{j+m_2},t_{j+1}) \\ \vdots & \vdots & \cdots & \vdots \\ G(t_{j+n-1},t_{j+n-1}) & G(t_{j+n},t_{j+n-1}) & \cdots & G(t_{j+m_2+n-2},t_{j+n-1}) \end{bmatrix}, \tag{3.6}$$

where n denotes the number of rows in t' we consider together. Note that the sampling window (I) is a special case of (II). It can be used in a DMD analysis to predict values of $G(t,t')$ to the right of the parallelogram region in the second step. However, the snapshot matrix used in this step is the transpose of the $\mathbf{X}$ matrix defined in (3.5).

As in this method, the k-point is always fixed, we call it fixed k-point (FK) DMD extrapolation.

3.3. Computational cost

We now compare the computational cost of HODMD with the cost of solving KBEs numerically on a two-time grid with $N \times N$ grid points. We assume n_k k-points are used to represent the Green's function. When the second-Born approximation is used to represent the self-energy, it is easy to show [5, 6], that the computational complexity for solving the KBE numerically is $O(n_k^3 N^3)$. The cubic scaling with respect to time (N^3) results from the evaluation of the collision integral in each time evolution step.

When DMD is used to construct a reduced order model, we need to first solve the KBEs in a small window $[0, t_m]$ (with $m < N$) numerically. The cost for this step is $O(n_k^3 m^3)$. If m is relatively small compared to N, this cost is considered a constant with respect to the final time.

The main computational cost of DMD is in the SVD of the matrix $\mathbf{X}_1$ in (2.4), which takes $O(n_k^2 m)$ operations in general when the matrix to be decomposed is of dimension $n_k \times m$. If we use HODMD[d_1] with m_1 snapshots in the first step of the FT-DMD procedure described in Section 3.1, and HODMD[d_2] with m_2 snap-

shots in the second step, the overall cost for constructing the reduced order model is $O(m_2 \min(n_k^2 d_1 m_1, n_k m_1^2/d_1))+$ $O(N \min(n_k^2 d_2 m_2, n_k m_2^2/d_2))$, which is linear with respect to N.

Similarly, if we use HODMD[d_1] with m_1 snapshots in the first step of the FK-DMD procedure described in Section 3.2, and HODMD[d_2] with m_2 snapshots in the second step, it takes $O(n_k \min(m_2^2 d_1 m_1, m_2 m_1^2/d_1)+$ $O(n_k \min(N^2 d_2 m_2, N m_2^2/d_2))$ operations to perform the SVDs required to construct the reduced order model.

Once reduce order models (2.10) are constructed, evaluating these models on $O(N^2)$ two-time grid points takes $O(n_k N^2)$ operations.

Therefore, for large N, the DMD based extrapolation can be significantly faster than solving the KBEs numerically as we will demonstrate in the next section. :q

4. Results and discussions

In this section, we demonstrate and compare methods for predicting the off-diagonal elements of $G(t, t')$ discussed in the previous section. All methods are applied to the two-band Hubbard model problem [38, 39, 40] in which the many-body Hamiltonian is given by

$$H_{\text{total}}(t) = H_{\text{s}} + H_{\text{ext}}(t). \tag{4.1}$$

In (4.1), H_{s} is the system Hamiltonian defined as

$$H_{\text{s}} = \frac{1}{2}\sum_{\mathbf{k}} (\epsilon_{v\mathbf{k}} c_{v\mathbf{k}}^\dagger c_{v\mathbf{k}} + \epsilon_{c\mathbf{k}} c_{c\mathbf{k}}^\dagger c_{c\mathbf{k}}) - U\sum_{k} c_{c\mathbf{k}}^\dagger c_{c\mathbf{k}} + \frac{U}{N_0}\sum_{\mathbf{k}_1,\mathbf{k}_2,\mathbf{q}} c_{v\mathbf{k}_1+\mathbf{q}}^\dagger c_{c\mathbf{k}_2-\mathbf{q}}^\dagger c_{c\mathbf{k}_2} c_{v\mathbf{k}_1}, \tag{4.2}$$

where $\epsilon_{v\mathbf{k}}$ ($\epsilon_{c\mathbf{k}}$) is the band energy of the valence (conduction) band with momentum $\mathbf{k}$, $U = 1$ is the on-site interaction between the two bands, and N_0 is the number of sites in the system. The energy dispersion is taken to be

$$\epsilon_{v\mathbf{k}} = -(1 - \cos(\mathbf{k})) - E_g/2$$
$$\epsilon_{c\mathbf{k}} = (1 - \cos(\mathbf{k})) + E_g/2,$$

with $E_g = 1$ the band gap. The second term in (4.1) is the light-matter coupling within the dipole approximation defined by

$$H_{\text{ext}}(t) = E(t)\sum_{\mathbf{k}} (d_{\mathbf{k}} c_{c\mathbf{k}}^\dagger c_{v\mathbf{k}} + d_{\mathbf{k}}^* c_{v\mathbf{k}}^\dagger c_{c\mathbf{k}}), \tag{4.3}$$

where $E(t)$ is the time-dependent intensity of the field that is uniform in real space and $d_{\mathbf{k}}$ is the dipole matrix element. For simplicity we set $d_{\mathbf{k}} = 1$.

The many-body Hamiltonian (4.1) describes how electrons and holes interact with each other and with a classical light field.

We seek to solve the KBE associated with the non-equilibrium many-body dynamics under this Hamiltonian. The single-particle Hamiltonian $H(t)$ in (1.1) is derived from the many-body perturbation theory and always contains the first-order Hartree-Fock self-energies

$$\Sigma_{cc}^{\text{Hartree}}(t) = -i\frac{U}{n_k}\sum_{\mathbf{k}} G_{vv}(\mathbf{k};t,t), \quad \Sigma_{vv}^{\text{Hartree}}(t) = -i\frac{U}{n_k}\sum_{\mathbf{k}} G_{cc}(\mathbf{k};t,t), \tag{4.4}$$

and

$$\Sigma_{cv}^{\text{Fock}}(t) = i\frac{U}{n_k}\sum_{\mathbf{k}} G_{cv}(\mathbf{k};t,t), \quad \Sigma_{vc}^{\text{Fock}}(t) = i\frac{U}{n_k}\sum_{\mathbf{k}} G_{vc}(\mathbf{k};t,t). \tag{4.5}$$

The Fock self-energy (4.5) in our example is independent of the momentum $\mathbf{k}$ since our onsite interaction U does not have $\mathbf{k}$-independence. The second-order self-energy $\Sigma(t,\bar{t})$ in (1.1) is approximated by the second-Born correction

$$\begin{aligned}\Sigma_{jm}^{\text{2B}}(\mathbf{k};t,t') =& \frac{U^2}{n_k^2}\sum_{ps}\sum_{\mathbf{qk}'} G_{ps}(\mathbf{k}'+\mathbf{q};t,t')G_{sp}(\mathbf{k}';t',t)G_{jm}(\mathbf{k}-\mathbf{q};t,t') \\ &- \frac{U^2}{n_k^2}\sum_{ps}\sum_{\mathbf{qk}'} G_{jp}(\mathbf{k}';t,t')G_{ps}(\mathbf{k}'-\mathbf{q};t',t)G_{sm}(\mathbf{k}-\mathbf{q};t,t'),\end{aligned}$$

where $G_{pq}(\mathbf{k};t,t')$ is the two-time Green's function with band indices p, q, and crystal momentum index $\mathbf{k}$. To compute the initial state, we set the system to half-filling with a fully occupied valence band and start from Hartree-Fock ground state in the calculation. As discussed in Section 1, the KBEs can be solved numerically by a Runge-Kutta type of time integrator in two times [10]. Before using DMD to predict the long-time behavior of the two-time Green's function $G(t,t')$, we first solve the KBEs by numerical time evolution within a relatively small two-time window, and use the numerical solution to construct data matrices required to perform a DMD.

In the following numerical examples, we assume that $E(t)$ is an instantaneous pulse given by $I\delta(t-0.5)$, where I denotes the pulse intensity, and $\delta(t-0.5)$ denotes a delta function centered at $t=0.5$. The Brillouin zone $[-\pi,\pi]$ is discretized uniformly by $n_k = 20$ k-points set to $k_s = -\pi + 2(s-1)\pi/n_k$ $(s=1,...,n_k)$. Our goal is to predict the values of $G(k_s;t,t')$ for $(t,t') \in [0,200]\times[0,200]$ on a uniform two-time grid (t_i,t_j), with $t_i = (i-1)\Delta t$ and $t_j = (j-1)\Delta t$ where $\Delta t = 0.1$, $i,\ j = 1,...,2001$. As a result, the number of time grid points in each time direction is $N = 2001$, and the total number of $G(k_s,t_i,t_j)$'s to be evaluated is $k_s \times N \times N = 20 \times 2001 \times 2001$. We will validate the predictions made by HODMD below against numerical solutions of the KBEs obtained from a method that is based on a second-order implicit Runge-Kutta method and a fixed point iteration. To check the accuracy of the computed G, we recomputed the solution in $t \in [0,50]$ using a smaller time step $\Delta t = 0.02$. Figures 4.1 shows the solution obtained from $\Delta t = 0.1$ matches well with that obtained from $\Delta t = 0.02$ when $I = 0.5$. We have similar observations when $I = 0.001$ and $I = 1.5$. In addition, we validated the correctness of the computed solution by checking the conservation of total energy as suggested in [13]. Figure 4.2 shows that the total energy is conserved in the limit of large t even though some fluctuation is observed for $t < 1$. We believe such fluctuation originates from the instantaneous injection of the external field. Our validation suggests that it is reasonable to use

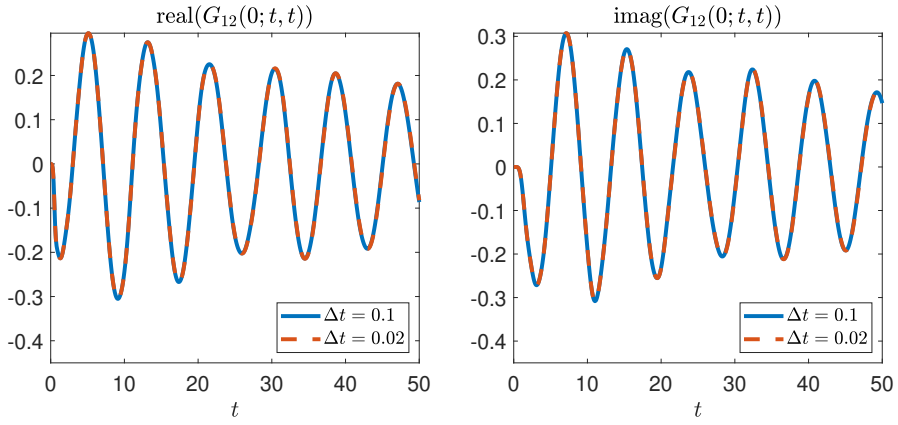

Figure 4.1: $I = 0.5$. Comparison of the numerical solutions with $\Delta t = 0.1$ and $\Delta t = 0.02$.

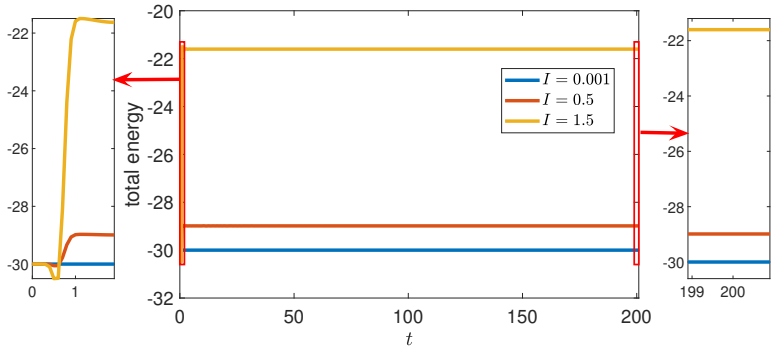

Figure 4.2: Change of the total energy in time t with different pulse intensities.

the numerical solution of the KBEs obtained with $\Delta t = 0.1$ as a baseline for comparison in the following numerical examples.

In all the numerical experiements presented below, we use HODMD instead of the standard DMD in order to compensate for the potential lack of spatial/momentum resolution in the sampled snapshots. Although we could improve the momentum resolution by generating more k-points, this approach would significantly increase computational and memory cost used to solve the KBE numerically (within the same two-time window.) [27]. Following the notation established in Section 2, we use HODMD[d] to denote the version of HODMD in which d consecutive snapshots of G (in some time direction) are combined into a single column of the snapshot matrix, and no overlap exists between two adjacent columns of the snapshot matrix, as defined in (2.13).

4.1. Predicting $G(k;t,t')$ for fixed $t-t'$

We first report the effectiveness of using HODMD to predict $G(k;t,t')$ for fixed $t-t'$ values, i.e., we predict the values of $G(k;t,t')$ along the time-diagonal and subdiagonals within the parallelogram outlined by the blue dashed lines in Figure 3.2. To predict the values of $G(k;t,t')$ for $t-t' = (j-1)\Delta t$, with $j \in \{1,2,...,m_2\}$, we use $G(k;t_i,t_{i-j+1})$ with $j \le i \le j+m_1-1$ to construct a snapshot matrix required in an HODMD calculation. Here the parameter m_2 is the total number of time-subdiagonals of $G(k;t,t')$ we will predict, and m_1 is the minimum number of snapshots we will use to perform the HODMD calculation. The HODMD calculation for each j is independent from the others, i.e., the HODMD calculations for different time-subdiagonals of G can be performed in parallel. In order to perform these HODMD calculations, we need to first solve the KBE numerically within the time window $[0,t_{m_1+m_2-1}]\times[0,t_{m_1+m_2-1}]$. As mentioned in Section 3.1, When $t-t' < (m_2-1)\Delta t$, more snapshots can be used in the HODMD analysis. In particular, for $t=t'$, we can use as many as m_1+m_2-1 snapshots.

Figure 4.3(a) shows the singular values of the snapshot matrix $\widetilde{\mathbf{X}}_1$ (2.13) constructed for $t-t' = 100\Delta t = 10$. The intensity of the external pulse in (4.3) is set to $I = 0.001$. We set m_1 to 100 to include at least 100 snapshots in the snapshot matrix $\mathbf{X}$, and use HODMD[4] to perform the extrapolation. In this case, the singular values of $\mathbf{X}$ decay rapidly. Only the leading 14 singular values are significantly larger than 0, indicating that the dynamics of $G(k;t+100\Delta t,t)$ can be well characterized by 14 DMD modes.

To assess the accuracy of the HODMD extrapolation, in Figure 4.3(b), we plot the correlation $|c_\ell|$ between the numerical solution of the KBE and the HODMD extrapolation along $(t+\ell\Delta t,t)$, which is defined by

$$c_\ell = \min_s \frac{\langle G(k_s;t+\ell\Delta t,t), G^{\mathrm{DMD}}(k_s;t+\ell\Delta t,t)\rangle}{\|G(k_s;t+\ell\Delta t,t)\|\|G^{\mathrm{DMD}}(k_s;t+\ell\Delta t,t)\|}, \quad \ell = 0,1,...,199, \tag{4.6}$$

where $G(k_s;t+\ell\Delta t,t)$ is obtained from the numerical solution of the KBE on a uniform two-time grid in $[0,200]\times[0,200]$, $G^{\mathrm{DMD}}(k_s;t+\ell\Delta t,t)$ is the extrapolated trajectory produced from HODMD, and $\langle\cdot,\cdot\rangle$ denotes the standard Euclidean inner product of two complex vectors. We note that c_ℓ is the cosine of the angle between the predicted and the computed trajectories. For each ℓ, we take the minimum of such cosine values among all k-points, which yields the largest difference between the extrapolated and the original trajectories among all k points. We can clearly see that for $m_1 = 100$ and $m_2 = 200$, the HODMD prediction is nearly perfect for $I = 0.001$.

When I is increased to 0.5, we perform an HODMD[5] extrapolation using $m_1 = 450$, which is the minimum number of snapshots required to produce satisfactory extrapolations along the diagonals, and $m_2 = 400$, which is the minimum number of snapshots required for each t' to produce a satisfactory extrapolation away from the diagonal (see Section 3). The singular values of the snapshot matrix for $G(k;t+100\Delta t,t)$ and the correlation $|c_\ell|$ between the numerical solution of the KBE and the HODMD prediction are similar to those shown in Figure 4.3 where $I = 0.001$. The only difference is that the snapshot matrix has more large singular values, indicating that the dynamics associated with $I = 0.5$ contains more momentum and temporal features than the dynamics associated with a smaller I. These additional features would need to

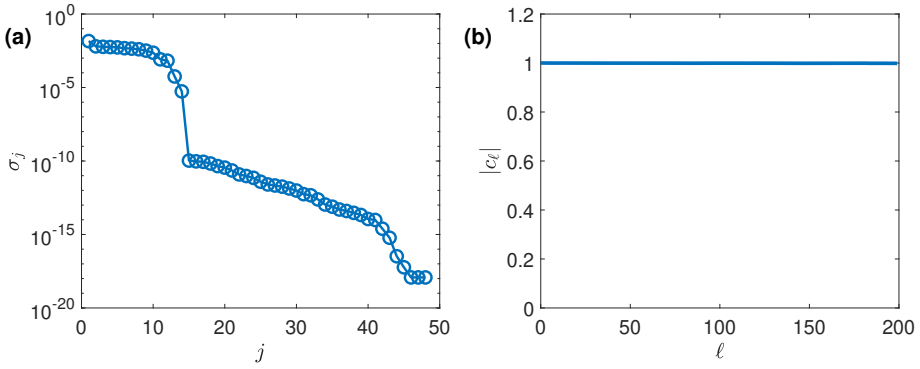

Figure 4.3: $I = 0.001$. **(a)** The singular values of the snapshot matrix $\widetilde{\mathbf{X}}_1$ (2.13) in HODMD[4] constructed from $G(k;(m+100)\Delta t, m\Delta t)$, for $m = 0, 1, ..., m_1 - 1 = 99$; **(b)** The correlation $|c_\ell|$ between the numerical solution of the KBE and the HODMD[4] extrapolation of G along $(t + \ell\Delta t, t)$, $\ell = 0, 1, ..., m_2 - 1 = 199$.

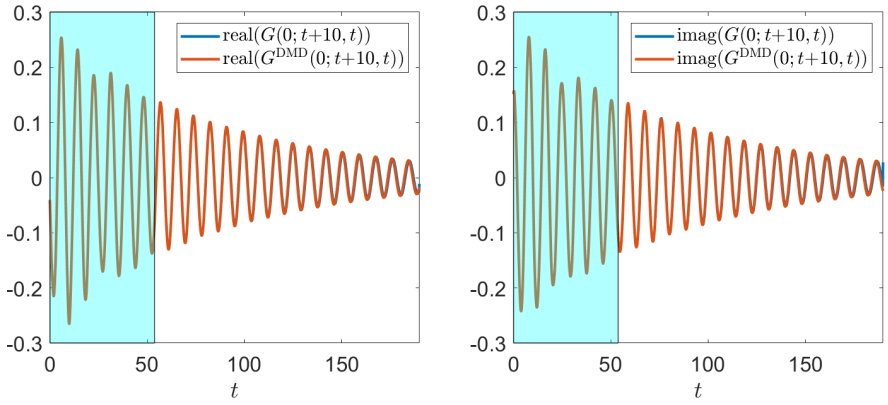

Figure 4.4: $I = 0.5$. The extrapolated $G(0; t + 10, t)$ by HODMD[5] where the snapshot matrix $\widetilde{\mathbf{X}}_1$ (2.13) is constructed from $G(k;(m+100)\Delta t, m\Delta t)$, for $m = 0, 1, ..., m_1 - 1 = 449$. The shaded region represents the window of sampled snapshots from the numerical solution of the KBE.

be accounted for by an approximate Koopman operator of a larger dimension and thus more terms in (2.9). With these terms, all the $m_2 = 400$ subdiagonals are accurately extrapolated as the values of $|c_\ell|$ are close to 1 for all ℓ. The extrapolated trajectory of the 100-th subdiagonal of G, i.e., $G^{\mathrm{DMD}}(0; t + 10, t)$ is plotted in Figure 4.4 and compared with the trajectory $G(0; t + 10, t)$ obtained from the numerical solution of the KBE. The sampled data are marked by the blue shaded window. We can observe that the extrapolated trajectory successfully captures the oscillating frequency and the decay rate of the amplitude.

To check the number of snapshots (m_1) required in the HODMD to accurately extrapolate $G(t + 10, t)$,

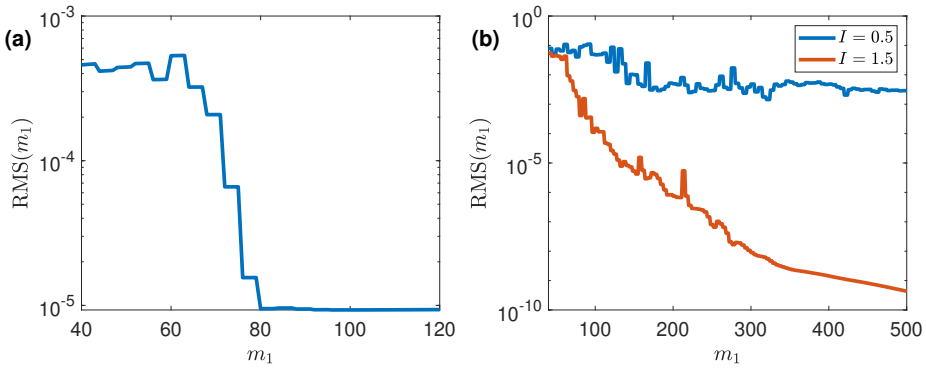

Figure 4.5: The root mean square errors RMS(m_1) for $G(k; t+10, t)$ when **(a)** $I = 0.001$; **(b)** $I = 0.5$ and $I = 1.5$.

we define the root mean square (RMS) error of the extrapolated trajectory as

$$\mathrm{RMS}(m_1) = \left[\frac{\sum_{j=1}^{n_k} \sum_{p=m_1+1}^{N-m_2+1} |G(k_j; t_{p+100}, t_p) - G^{\mathrm{DMD}}(k_j; t_{p+100}, t_p)|^2}{n_k(N - m_1 - m_2 + 1)} \right]^{1/2}, \tag{4.7}$$

where we set the value of m_2 to 101. The extrapolation is computed by HODMD[4] when $I = 0.001$, HODMD[5] when $I = 0.5$ and HODMD[4] when $I = 1.5$. The corresponding RMS errors are plotted in Figure 4.5.

As we can see from Figure 4.5(a), the RMS for the extrapolated $G(t+10, t)$ starts to decrease rapidly when $m_1 > 60$ and levels off around $m_1 = 80$ in the $I = 0.001$ case. The magnitude of RMS matches that of the numerical integration error contained in the numerical solution of the KBE. When $I = 0.5$, the RMS starts to decrease from 10^{-1} to 10^{-2}, which is the expected level of error in the numerical solution of KBE when $m_1 > 120$. When $I = 1.5$, the RMS starts to decrease rapidly when $m_1 > 50$, when $m_1 = 500$, the RMS is on the order of 10^{-10}. This is due to the fact that the magnitude of $G(t+10, t)$ rapidly decreases towards 0 when t increases.

4.2. Predicting $G(k; t, t')$ for fixed t'

As discussed in Section 3, to predict the values of the two-time Green's function outside of the m_2 subdiagonal bands in (t, t'), we can use HODMD to extrapolate $G(k; t, t')$ horizontally on the two-time grid by fixing t' in G. For each fixed $t' = t_j$, we use either the computed or extrapolated values of $G(k; t_i, t_j)$, for $j \le i \le j + m_2 - 1$ to construct a snapshot matrix from which DMD modes can be extracted to extrapolate the values of $G(k; t_i, t_j)$ for $j + m_2 \le i \le N$.

The accuracy of the prediction can be assessed by examining the correlation between the extrapolated Green's function, denoted by $G^{\mathrm{DMD}}(k; t, t')$ and the numerical solution of the KBE denoted by $G(k; t, t')$ along a fixed t' defined as

$$c^k(t') = \frac{\langle G(k; t, t'), G^{\mathrm{DMD}}(k; t, t') \rangle}{\|G(k; t, t')\| \|G^{\mathrm{DMD}}(k; t, t')\|}, \quad k = k_s, \quad s = 1, ..., n_k. \tag{4.8}$$

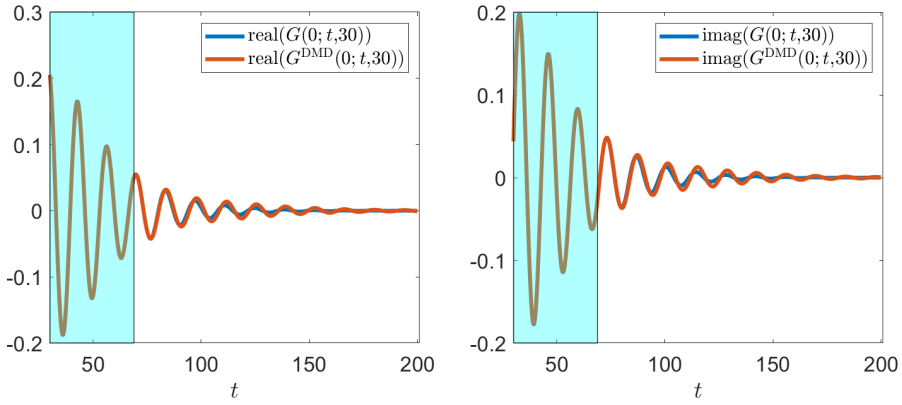

Figure 4.6: $I = 0.5$. A comparision between the real and imaginary parts of $G^{\mathrm{DMD}}(0;t,30)$ and $G(0;t,30)$ by HODMD[10] with those of $G(0;t,30)$. The shaded area marks time window from which snapshots are used to construct the HODMD model.

When the intensity of the external field $E(t) = I\delta(t)$ in (4.3) is set to $I = 0.5$, we found $c^k(30)$ are close to 1.0 for nearly all k-points. This agreement is confirmed in Figure 4.6 where we show the real and imaginary parts of $G^{\mathrm{DMD}}(0;t,30)$ match well with those of $G(0;t,30)$.

We make a similar comparison between $G(k;t,120)$ and $G^{\mathrm{DMD}}(k;t,120)$ in Figure 4.7. Note that, in this case, the snapshot matrix used in HODMD is constructed from the extrapolated values of $G(k,t_j,120)$, $120 \le t_i \le 120 + m_2 - 1$, obtained in a previous HODMD step, in which $m_2 = 400$ subdiagonal lines of $G(k;t,t')$ are extrapolated from the numerical solution of the KBE within $[0,84.9]\times[0,84.9]$. The correlation factor $|c^k(120)|$ deviates slightly from 1.0 for some k values. Such small deviations can also be seen in Figure 4.7 where we plot both the real and imaginary parts of $G(0;t,120)$ and $G^{\mathrm{DMD}}(0;t,120)$. We believe these small deviations are caused by small extrapolation errors introduced in the previous step in which HODMD is used to extraploate $G(k;t,t')$ along the diagonal and subdiagonals of the two-time grid.

In Section 3, we also discussed the possibility to extrapolate $G(k;t,t')$ horizontally from the numerical solution of the KBE in the time window $[0,t_m]\times[0,t_m]$ directly for $t' < t_m$ without constructing an HODMD model to extrapolate along the diagonal and subdiagonals of the two-time window first. We now examine the effectiveness of this approach.

Because the solution to the KBE is computed for $t \ge t'$ within $[0,t_m]\times[0,t_m]$, the larger the t', the fewer data points we can use to construct the snapshot matrix. However, by making use of the following symmetric property of the Green's function [5], i.e.,

$$G_{b_1,b_2}(k;t,t') = -\overline{G_{b_2,b_1}(k;t',t)}, \tag{4.9}$$

where b_1 and b_2 denote the band indices, we can augment the snapshot matrix $G_{12}(k;t,t')$ for a fixed t' with samples of $-\overline{G_{b_2,b_1}(k;t',t)}$. Unfortunately, such a symmetry exploiting data augmentation scheme is not always satisfactory as we will see below.

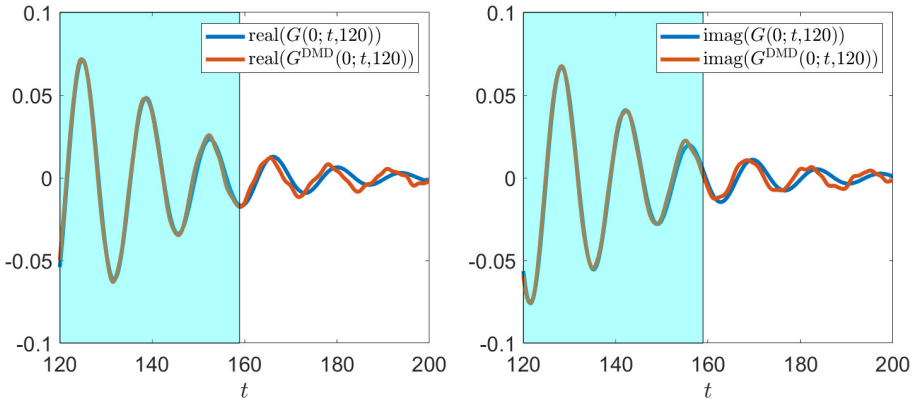

Figure 4.7: $I = 0.5$. A comparision between the real and imaginary parts of $G^{\mathrm{DMD}}(0;t,120)$ and $G(0;t,120)$ by HODMD[10] with those of $G(0;t,120)$. The shaded area marks time window from which snapshots are used to construct the HODMD model.

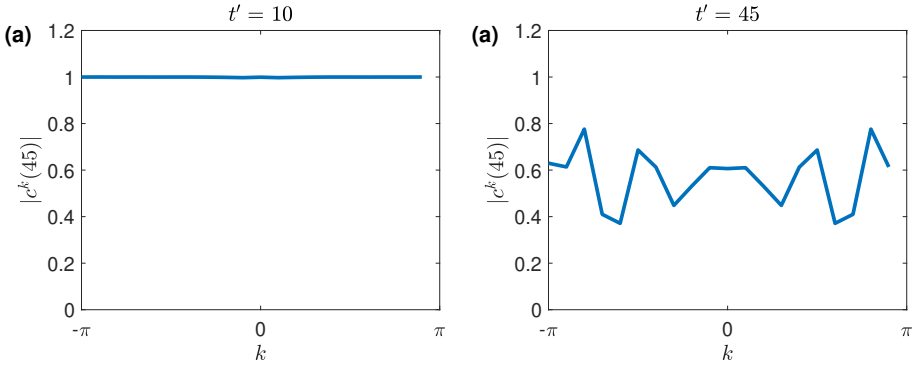

Figure 4.8: $I = 0.5$. **(a)** The correlation $|c^k(10)|$ between $G^{\mathrm{DMD}}(k;t,10)$ and $G(k;t,10)$; **(b)** The correlation $|c^k(45)|$ between $G^{\mathrm{DMD}}(k;t,45)$ and $G(k;t,45)$.

In the following example with $I = 0.5$, we set m to 500, i.e., we first solve the KBE within the time window of $[0,t_{500}]\times[0,t_{500}] = [0,49.9]\times[0,49.9]$. We use the values of computed $G_{12}(k;t,10)$ and $G_{12}(k;t,45)$ within this time window to construct snapshot matrices that can be used in HODMD[6] to extrapolate $G_{12}(k;t,10)$ and $G_{12}(k;t,45)$ for $t > 49.9$, as shown in Figure 3.4.

The singular values of both snapshot matrices decrease rapidly, and there are around 65 dominant singular values with a clear gap between these singular values and the others.

However, Figure 4.8 shows that the two (time) slices of the extrapolated Green's functions exhibit different accuracy features. At $t' = 10$, the correlation between the HODMD extrapolation $G^{\mathrm{DMD}}(k;t,10)$ and the corresponding $G(k;t,10)$ obtained from the numerical solution of the KBE is nearly perfect at all k-points. Much lower correlation is observed between $G^{\mathrm{DMD}}(k;t,45)$ and $G(k;t,45)$.

The excellent agreement between $G^{\mathrm{DMD}}(k;t,10)$ and $G(k;t,10)$ and the lack of satisfactory agreement

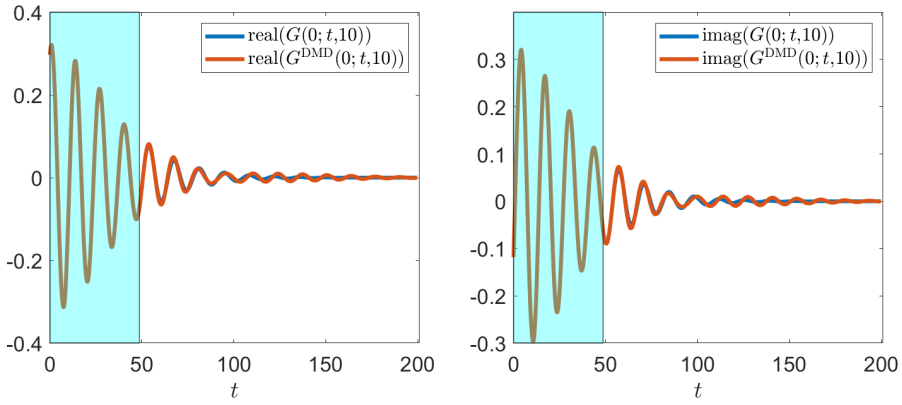

Figure 4.9: $I = 0.5$. The extrapolated $G(0;t,10)$ by HODMD[6] with the snapshot matrix $\widetilde{\mathbf{X}}_1$ constructed from $G(k;n\Delta t,10)$, for $n = 0,1,..,m_2-1 = 499$. The shaded area marks time window from which snapshots are used to construct the HODMD model.

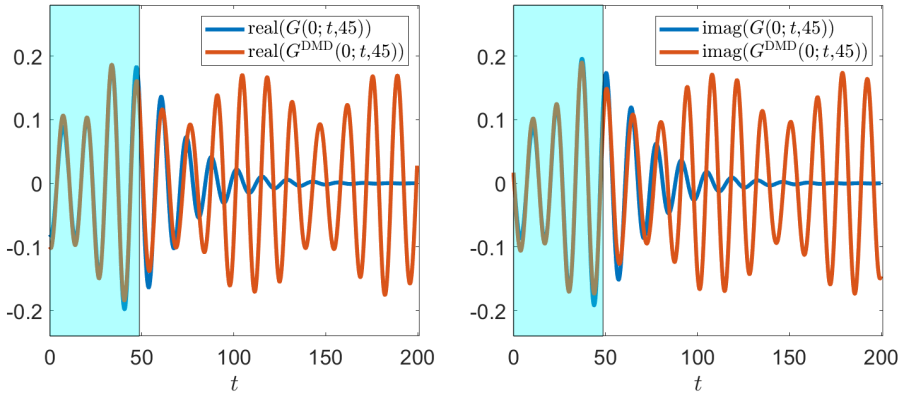

Figure 4.10: $I = 0.5$. The extrapolated $G(0;t,45)$ by HODMD[6] with the snapshot matrix $\widetilde{\mathbf{X}}_1$ constructed from $G(k;n\Delta t,45)$, for $n = 0,1,..,m_2-1 = 499$. The shaded area marks time window from which snapshots are used to construct the HODMD model.

between $G^{\mathrm{DMD}}(k;t,45)$ and $G(k;t,45)$ are confirmed in Figures 4.9 and 4.10 where we plot both the real and imaginary parts of the computed and extrapolated $G(0;t,10)$ and $G(0;t,45)$, respectively. In particular, at $t' = 10$, the HODMD extrapolation correctly captures both the decay amplitude and oscillation frequencies of $G(0;t,10)$. However, at $t' = 45$, the extrapolated $G^{\mathrm{DMD}}(0;t,45)$ deviates significantly from the solution of the KBE.

We believe that the reason HODMD performs poorly in predicting the values of $G(k;t,45)$ for $t > 49.9$ is that an accurate HODMD model requires a sufficiently large number of snapshots $G(k;t_i,t')$ for $t_i \geq t'$.

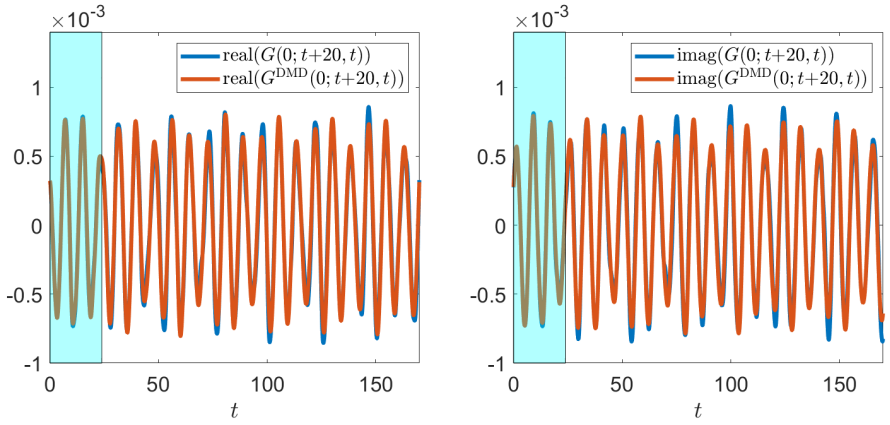

Figure 4.11: $I = 0.001$. A comparison of $G^{\mathrm{DMD}}(0; t+20, t)$ with $G(0; t+20, t)$. The extrapolation is computed by HODMD[10] with the snapshot matrix $\widetilde{\mathbf{X}}_1$ constructed from $G(0; (p+q)\Delta t, p\Delta t)$ with $p = 0, 1, ..., m_2 - 1 = 299$ and $q = 0, 1, ..., m_1 - 1 = 249$. The shaded area marks the time window from which snapshots are used to construct the HODMD model.

In this experiment, only 50 snapshots within $[45, 50]$ are available for using in HODMD, which is apparently not enough to construct an accurate reduced order model.

4.3. Predicting $G(k; t, t')$ for a fixed k

We now report the effectiveness of an alternative DMD extrapolation scheme discussed in Section 3.2. In this scheme, we use snapshots of $G(k; t, t')$ within a small two-time window for a fixed k to construct a DMD-based reduced order model from which values of $G(k; t, t')$ are predicted for large t and t'.

In the first numerical example, we set the intensity of the external field to $I = 0.001$ and solve the KBE within the two time window $[0, 54.9] \times [0, 54.9]$. We then set $m_1 = 250$, $m_2 = 300$ and construct a snapshot matrix $\mathbf{X}$ for each k according to (3.5). We use HODMD[10] to construct a reduced order model to extrpolate values of $G(k; t, t')$ along the diagonal and subdiagonals of the two time grid for $t - t' \leq 24.9$.

Figure 4.11 shows that for $k = 0$ and $t - t' = 20$, the extrapolated $G^{\mathrm{DMD}}(0, t + 20, t)$ agrees well with the computed $G(0; t + 20, t)$ obtained from the numerical solution of the KBE. Similar good agreements are observed for other $t - t'$ and k values.

Following the strategy presented in Section 3.2, once we extrapolate $G(k; t, t')$ along the diagonal and subdiagonals for each k, we then partition the parallelogram formed by the subdiagonal bands on a two-time grid vertically into several strips of size $n \times m_2$. In this experiment, we choose $n = 30$ and $m_2 = 300$. The computed or extrapolated values of $G(k; t, t')$ values within each strip are used to construct a snapshot matrix $\mathbf{X}$ according to (3.6). HODMD[2] is performed to construct a reduced order model from which the values of $G(k; t, t')$ outside of the subdiagonal band of width m_2 can be extrapolated.

Figure 4.12 shows that, for $k = 0$ and $t' = 120$, the extrapolated $G^{\mathrm{DMD}}(0, t, 120)$ agrees well with the computed $G(0; t, 120)$ obtained from the numerical solution of the KBE. Note that in this case, the snapshot

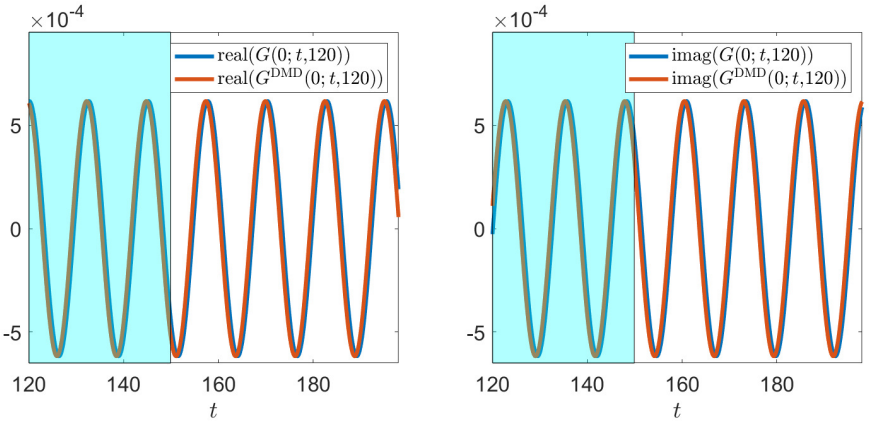

Figure 4.12: $I = 0.001$. A comparison of $G^{\mathrm{DMD}}(0;t,120)$ with $G(0;t,120)$. The extrapolation is computed by HODMD[2] with the snapshot matrix $\widetilde{\mathbf{X}}_1$ constructed from $G(0;120+(p+q)\Delta t, 120+p\Delta t)$ with $p = 0,1,...,n-1 = 29$ and $q = 0,1,...,m_2-1 = 299$. The shaded area marks the time window from which snapshots are used to construct the HODMD model.

matrix $\mathbf{X}$ is constructed from the extrapolated values of $G(0,t,t')$ along the subdiagonals of the two-time grid in the previous step. Similar good agreements are observed for other t' and k values.

These m_1 and m_2 values used in the above experiments appear to be the minimal required to produce accurate extrapolations both along the diagonals and off-diagonals. The choice of $n = 30$ is somewhat arbitrary. We observe that the extrapolation in the t direction is accurate for several values of $n \in [10, 1000]$.

When we increase the intensity of the external field to $I = 0.5$, we need to increase the value of m_1 to $m_1 = 450$ in order to obtain accurate extrapolation of $G(k;t,t')$ along the $m_2 = 300$ subdiagonals of the two-time grid. We use HODMD[10] to construct the reduced order model used to extrapolate $G(k,t,t')$ along the subdiagonals of the two-time grid for each k. The correlation $|c^k|$ between $G^{\mathrm{DMD}}(k;t+20,t)$ and $G(k;t+20,t)$ (obtained from the numerical solution of the KBE) is shown for all k-points in Figure 4.13(a). Although the correlations for the first 5 and the last 4 k-points appear to be somewhat low, the extrapolation appears to be accurate outside the time window that contains the sampled snapshots, as shown in Figure 4.14. This observation suggests that, for a fixed k, the long-time dynamics of $G(k;t,t')$ can be well approximated by a linear reduced order model along a fixed $t-t'$ for $t-t' \leq 29.9$, even though the model does not quite fit $G(k;t,t')$ for small t and t' on which $G(k;t,t')$ behaves more nonlinearly due to the onset of a higher intensity pulse. Since the values of $G(k;t,t')$ are already available from the numerical solution of the KBE for small t and t', and because we are mainly interested in the dynamics of G for large t and t', the extrapolation produced by HODMD[10] in this case is acceptable.

The extrapolation of G away from the diagonal for $t' = 120$ is shown in Figure 4.15. Compared to Figure 4.7, the extrapolated $G^{\mathrm{DMD}}(0;t,120)$ produced here is much closer to the numerical solution of the KBE than that produced by the extrapolation described in Section 4.2.

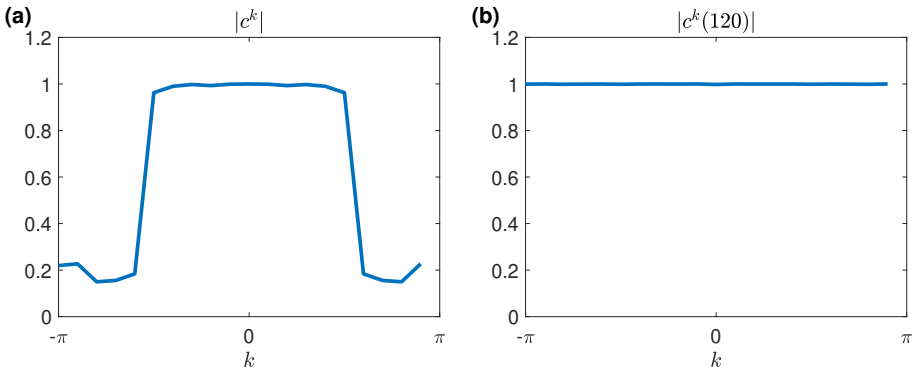

Figure 4.13: $I = 0.5$. **(a)** The correlation $|c^k|$ between the numerical solution of the KBE and the HODMD[10] extrapolation of $G(k; t + 20; t)$. The snapshot matrix $\widetilde{\mathbf{X}}_1$ is constructed from $G(k; (p + q)\Delta t, p\Delta t)$ with $p = 0, 1, ..., m_2 - 1 = 299$ and $q = 0, 1, ..., m_1 - 1 = 449$; **(b)** The correlation $|c^k(120)|$ between the numerical solution of the KBE and the HODMD[5] extrapolation of $G(k; t, 120)$. The snapshot matrix $\widetilde{\mathbf{X}}_1$ is constructed from $G(k; 120 + (p + q)\Delta t, 120 + p\Delta t)$ with $p = 0, 1, ..., n - 1 = 29$ and $q = 0, 1, ..., m_2 - 1 = 299$.

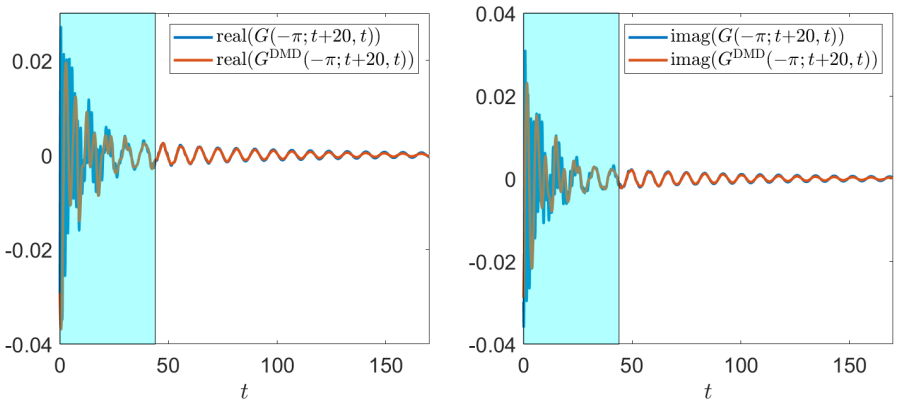

Figure 4.14: $I = 0.5$. A comparison of $G^{\mathrm{DMD}}(-\pi; t+20, t)$ with $G(-\pi; t+20, t)$. The extrapolation is computed by HODMD[10] with the snapshot matrix $\widetilde{\mathbf{X}}_1$ constructed from $G(-\pi; (p+q)\Delta t, p\Delta t)$ with $p = 0, 1, ..., m_2-1 = 299$ and $q = 0, 1, ..., m_1-1 = 449$. The shaded area marks the time window from which snapshots are used to construct the HODMD model.

When I is further increased to $I = 1.5$, we use HODMD[6] and HODMD[5] to extrapolate along the subdiagonal bands and away from the diagonal. In the first step, we take $m_1 = 80$ snapshots, while in the second step, we take $m_2 = 120$ snapshots. Extrapolation results at $k = 0$ for $G(0; t + 10, t)$ from the first step and $G(0; t, 12)$ from the second step are given in Figures 4.16 and 4.17, respectively. From Figure 4.16, we notice that, although there is not a complete oscillation period in the sampled window, HODMD gives a good approximation to the magnitude and frequency of the oscillation for large t and t'. Furthermore, for $t' = 12$, which falls out of the sampled window in the first step, the extrapolation from the second step matches well with the numerical solution of KBE. This agreement can be observed from Figure 4.17.

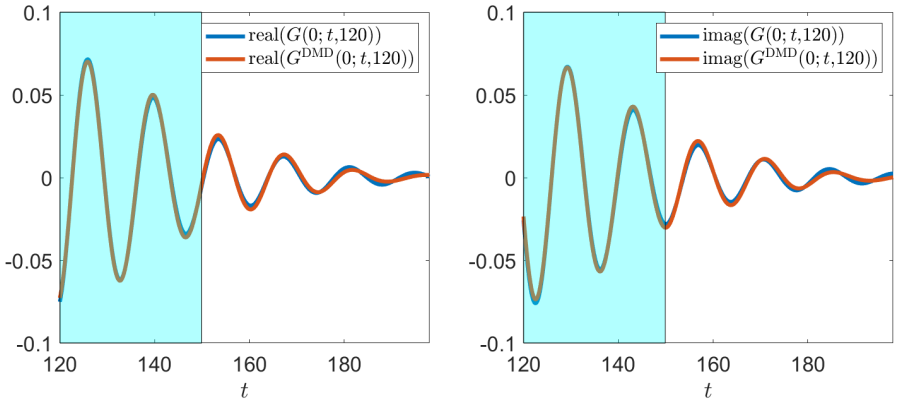

Figure 4.15: $I = 0.5$. A comparison of $G^{\mathrm{DMD}}(0;t,120)$ with $G(0;t,120)$. The extrapolation is computed by HODMD[5] with the snapshot matrix $\widetilde{\mathbf{X}}_1$ constructed from $G(0;120+(p+q)\Delta t, 120+p\Delta t)$ with $p = 0,1,...,n-1 = 29$ and $q = 0,1,...,m_2-1 = 299$. The shaded area marks the time window from which snapshots are used to construct the HODMD model.

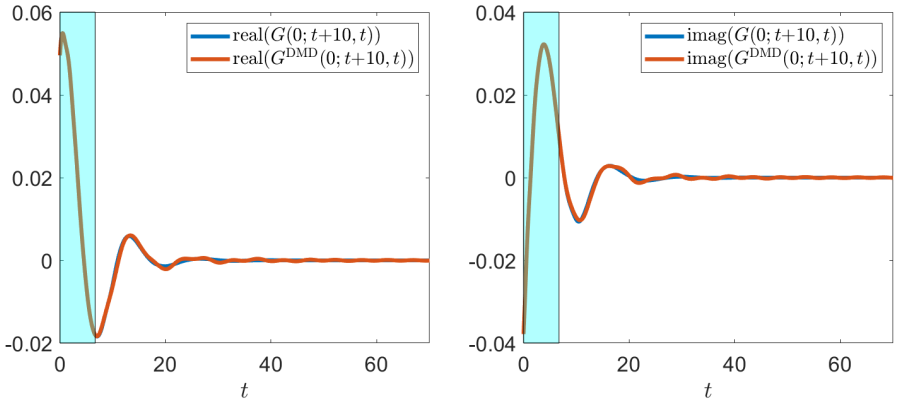

Figure 4.16: $I = 1.5$. A comparison of $G^{\mathrm{DMD}}(0;t+10,t)$ with $G(0;t+10,t)$. The extrapolation is computed by HODMD[6] with the snapshot matrix $\widetilde{\mathbf{X}}_1$ constructed from $G(0;(p+q)\Delta t, p\Delta t)$ with $p = 0,1,...,m_2-1 = 119$ and $q = 0,1,...,m_1-1 = 79$. The shaded area marks the time window from which snapshots are used to construct the HODMD model.

4.4. Spectral function and band structure approximation

Once $G(k;t,t')$ is available, we can use it to evaluate the time-dependent spectral function. The spectral function associated with $G = G_{11} + G_{22}$ at a particular k-point k can be computed by the formula

$$A(T,k,\omega) = \mathrm{imag}\left(\int_{t_0}^{T} dt_2 \int_{t_0}^{T} dt_1 s(t_2)s(t_1)e^{i\omega(t_1-t_2)}G(k;t_1,t_2)\right), \tag{4.10}$$

where

$$s(t) = e^{-\frac{(t-(T+\Delta t)/2)^2}{2(1000\Delta t)^2}}. \tag{4.11}$$

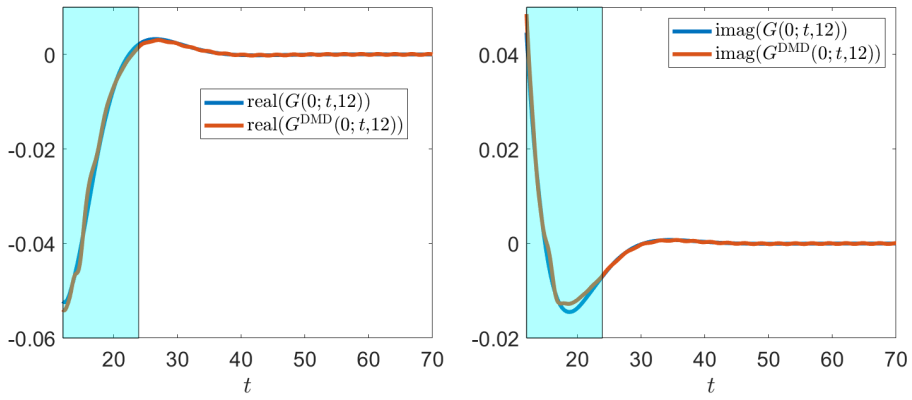

Figure 4.17: $I = 1.5$. A comparison of $G^{\mathrm{DMD}}(0;t,12)$ with $G(0;t,12)$. The extrapolation is computed by HODMD[5] with the snapshot matrix $\widetilde{\mathbf{X}}_1$ constructed from $G(0;12+(p+q)\Delta t, 12+p\Delta t)$ with $p = 0,1,...,n-1 = 29$ and $q = 0,1,...,m_2-1 = 119$. The shaded area marks the time window from which snapshots are used to construct the HODMD model.

In the formulas, $s(t)$ is the envelope function which describes the finite pulse duration of the probe light in the experiment, and t_0 is chosen so that we can get a smooth spectral function $A(T,k,\omega)$. Specifically, in our examples, we just take $t_0 = 0$. We can evaluate (4.10) numerically by first performing a discrete Fourier transform with respect to t_1 and using the trapezoid rule to evaluate the integral with respect to t_2.

By assembling spectral functions at multiple k-points, we can plot the band structure. In Figure 4.18, we compare the band structures $A(149.9,k,\omega)$, plotted as a heatmap, obtained from the numerical solution of the KBE as well as the extrapolated two-time Green's function $G^{\mathrm{DMD}}(t,t')$ for $I = 1.5$. The extrapolated Green's function is obtained by using the fixed timeline (FT) scheme discussed in Section 3.2. The fixed k-point (FK) extrapolation yields a nearly identical result and is not shown here for simplicity. We can clearly see that the band structure constructed from the $G^{\mathrm{DMD}}(t,t')$ is nearly indistinguishable from that constructed from the numerical solution of the KBE. Similar results are observed for band structures constructed from external fields with different intensities, i.e. $I = 0.001$ and $I = 0.5$.

In Figure 4.19, we take a closer look at the spectral functions at $k = 0$ (the central slice in Figure 4.18). We compare $A_{\mathrm{FT}}^{\mathrm{DMD}}$ with $A_{\mathrm{FK}}^{\mathrm{DMD}}$, and observe that they both match well with the spectral function obtained from the numerical solution of the KBE for $I = 0.5$ and $I = 1.5$. In particular, all major peaks of the spectral function are captured accurately. Remarkably, the small discrepancy between the extrapolated and the computed Green's functions shown in Figure 4.7 has very little effect on the accuracy of the spectral function.

To determine how the accuracy of HODMD extrapolation is affected by the number of snapshots we need to collect in both FT and FK based HODMD methods, we examine the RMS error of the spectral function

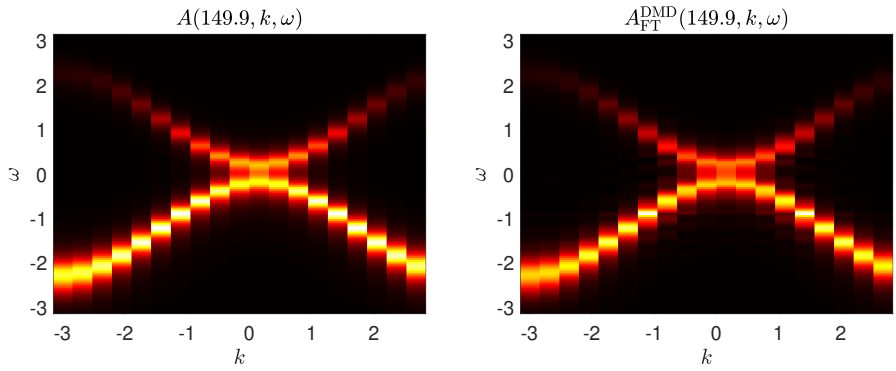

Figure 4.18: A comparison of band structure constructed from the numerical solution of the KBE for two-band model problem defined by (4.1) and (4.3) with $I = 1.5$, and a fixed k-point DMD extrapolation.

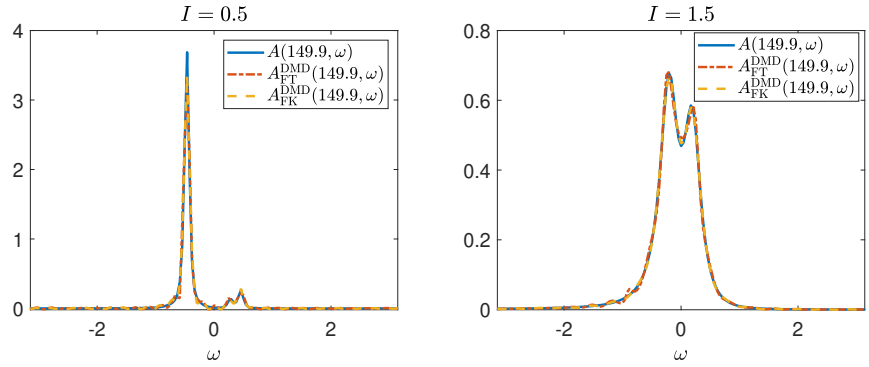

Figure 4.19: Comparisons of the spectral functions at $k = 0$ and $T = 149.9$ in (4.10) computed from the KBE solution and two types of DMD approximation when the coupling density $I = 0.5$ (left) and $I = 1.5$ (right).

for a particular choice of m_1 and m_2, defined as

$$\mathrm{RMS}_{\mathrm{method}}(m_1, m_2) = \frac{2\pi}{T + \Delta t} \sqrt{\sum_{\ell=0}^{T/\Delta t} \left(A(T, \omega_\ell) - A_{\mathrm{method}}^{\mathrm{DMD}}(T, \omega_\ell) \right)^2}, \quad j = 1, 2, \tag{4.12}$$

where 'method' is either FT or FK, and

$$\omega_\ell = -\frac{\pi}{\Delta t} + \frac{2\ell\pi}{T + \Delta t}, \quad \ell = 0, ..., \frac{T}{\Delta t} = 1499. \tag{4.13}$$

We plot $\mathrm{RMS}_{\mathrm{FT}}(m_1, m_2)$ and $\mathrm{RMS}_{\mathrm{FK}}(m_1, m_2)$ for several values of m_1 and m_2 between 100 and 500 in Figures 4.20-4.22 for $I = 0.001$, $I = 0.5$ and $I = 1.5$ respectively. Overall, we can observe that the RMS error decreases as m_1 and m_2 increase. When a sufficiently large set of m_1 and m_2 values are chosen, we observe that A_{FK} tends to be more accurate than A_{FT}. This observation is also consistent with what we observed in Figures 4.7 and 4.15, where the fixed k-point based HODMD extrapolation outperforms the fixed timeline based extrapolation.

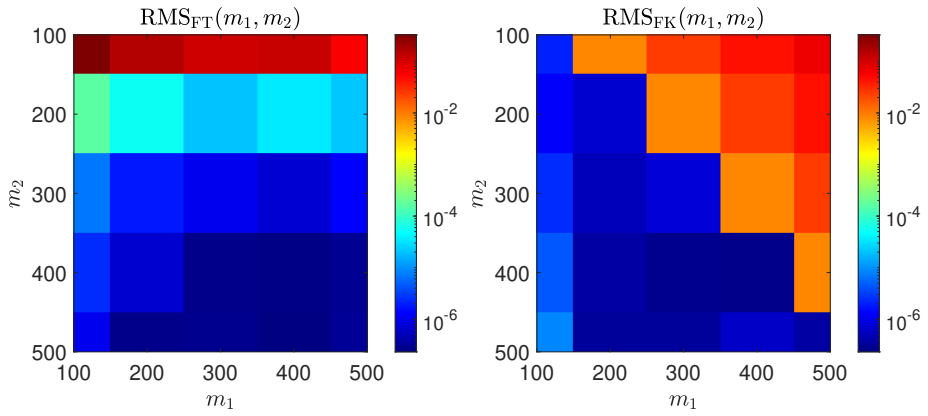

Figure 4.20: $I = 0.001$. The l_2-error (4.12) for the spectral function computed from the two HODMD extrapolated Green's function introduced in Sections 3.1 and 3.2 respectively.

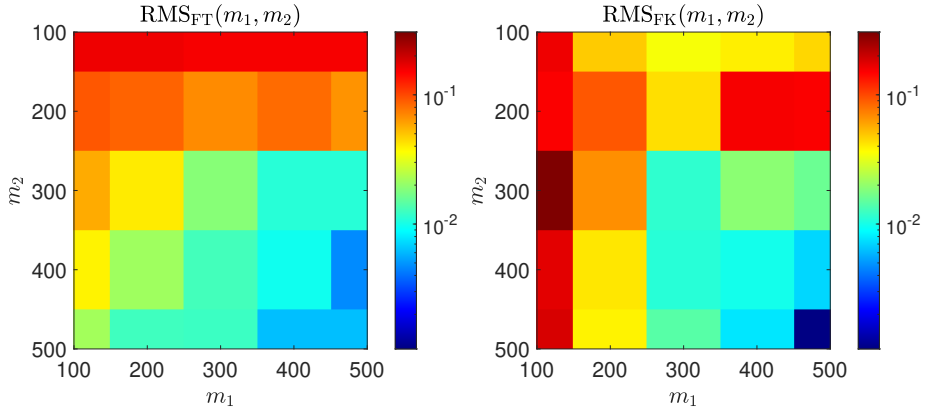

Figure 4.21: $I = 0.5$. The l_2-error (4.12) for the spectral function computed from the two HODMD extrapolated Green's function introduced in Sections 3.1 and 3.2 respectively

We observe in Figure 4.20 that $\mathrm{RMS}_{\mathrm{FK}}(m_1, m_2)$ is relatively large when $m_2 < m_1$ regardless how large m_2 is. We are not clear at the moment why m_2 must be larger than m_1 in this case.

4.5. Computational efficiency

In this section, we report the performance gain achieved by using DMD to extrapolate the non-equilibrium Green's function from the solution of the KBE within a small two-time window. As mentioned before, we use the numerical method presented in [5, 6] to solve the KBE associated with a two-band Hubbard model problem with second-Born approximation to the self-energy. The computation is carried out on Cori KNL computer maintained at NERSC. Message Passing Interface (MPI) is used to distribute Green's functions at

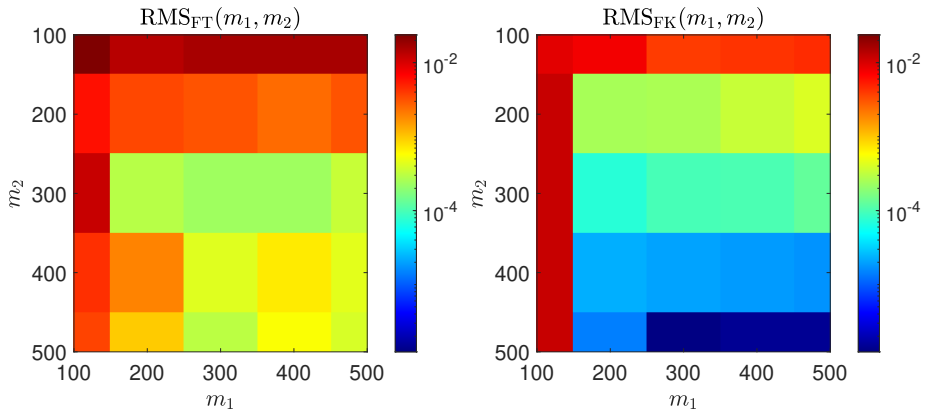

Figure 4.22: $I = 1.5$. The l_2-error (4.12) for the spectral function computed from the two HODMD extrapolated Green's function introduced in Sections 3.1 and 3.2 respectively

different k-points among different MPI ranks. These Green's functions can be updated in parallel. However, the evaluation of the self-energy and the integral term of the KBE requires global communication. For 20 k-points distributed among 20 MPI ranks, and wall clock minutes required to perform 500, 1000 and 2000 steps of time evolution respectively are listed in Table 4.1.

Number of time steps	500	1000	2000
wall clock time (min)	13	97	821

Table 4.1: The wallclock time used to perform numerical time evolution of the KBE on 20 MPI ranks.

From this table, we can clearly see the $O(t^3)$ scaling of the computational cost for solving the KBE. In fact, for this relatively small problem, performing 2000 steps of time evolution takes nearly 14 wall clock hours on 20 MPI ranks.

The use of DMD can significantly reduce the computational time and memory cost. As we indicated earlier, for $I = 0.001$ and $I = 1.5$, we can use DMD to extrapolate the entire Green's function from the numerical solution of the KBE within a small time window by performing only 500 steps of time evolution.

The wall clock time used to perform a fixed timeline (FT) DMD extrapolation on 20 MPI ranks is less than one minute. On the other hand, a fixed k-point DMD extrapolation can be done within 10 seconds. These time costs are negligible compared to the time required to solve the KBE. As a result, the use of DMD can speedup the entire computation by a factor of $821/14 \approx 59$.

For $I = 0.5$, we need to perform 1000 steps of time evolution before applying DMD extrapolation. The DMD extrapolation can still be completed in less one minute which results in a speedup of $821/98 \approx 8$.

Moreover, by reducing the number of time steps used to solve the KBE, we can reduce the memory cost

for storing each self-energy function from 5GB to 320MB.

5. Conclusion

In this paper, we applied the dynamic mode decomposition (DMD) method (and a variant called HODMD), which is a data-driven model order reduction technique, to predict the long-time dynamics of the two-time nonequilibrium Green's function from the numerical solutions of the Kadanoff-Baym equations (KBEs) within a small time window. While the original DMD is applicable to one-time dynamics only, we successfully used it to extrapolate two-time nonlinear dynamics by decomposing the two-time Green's function into several one-time functions in two different time directions. We presented two different time partitioning schemes and compared their effectiveness through numerical examples. We also presented a scheme in which one of the time variable is treated as a spatial variable at a fixed momentum grid point. Our numerical results show that this scheme can sometimes provide a more accurate prediction of the two-time Green's function in a large two-time window. We have also demonstrated that the DMD extrapolated Green's function can be used to compute interesting physical observables such as the band structure and the spectral functions of the many-body system accurately. By applying DMD/HODMD, we can significantly reduce the computational cost for computing these quantities because we do not need to solve the KBEs within a large two-time window. The cost of performing DMD and HODMD is negligible compared to the cost of solving the KBEs.

We remark here that there are other techniques to reduce computational complexity of solving the KBEs. One of these techniques uses the generalized Kadanoff-Baym ansatz (GKBA) [41, 42] to approximate and store the time diagonal of the Green's function first and use this one-time function together with Hatree-Fock propagators to obtain approximations to two-time Green's functions. Other techniques include the recently developed G1$-$G2 scheme [43]. These approaches use certain approximations of the collision integrals. In many cases, they have been shown to be sufficiently accurate. However, more systematic comparisons and evaluations need to be made. In these methods, DMD and HODMD can still be used to predict the long-time dynamics on one-time functions. We plan to study these methods and compare them with using DMD/HODMD based reduced order models for predicting non-equilibrium two-time Green's functions in the future.

Acknowledgments

This work is supported by the Center for Computational Study of Excited-State Phenomena in Energy Materials (C2SEPEM) at the Lawrence Berkeley National Laboratory, which is funded by the U. S. Department of Energy, Office of Science, Basic Energy Sciences, Materials Sciences and Engineering Division, under Contract No. DE-AC02-05CH11231, as part of the Computational Materials Sciences Program. The authors acknowledge the computational resources of the National Energy Research Scientific Computing (NERSC) center.

References

[1] G. Baym, L. P. Kadanoff, Conservation laws and correlation functions, Physical Review 124 (2) (1961) 287.

[2] L. P. Kadanoff, G. Baym, Quantum statistical mechanics: Green's function methods in equilibrium and nonequilibrium problems, CRC Press, 2018.

[3] L. Keldysh, Diagram technique for nonequilibrium processes, Soviet Physics JETP 20 (4) (1965) 1018–1026.

[4] A. Fetter, J. Walecka, Quantum Theory of Many-Particle Systems, McGraw-Hill Book Company, New York, 1971.

[5] K. Balzer, Nonequilibrium Green's Function Approach to Artificial Atoms, Ph.D. thesis, Inst. für Theoretische Physik und Astrophysik der Christian-Albrechts-Univ. (2007).

[6] A. Stan, N. Dahlen, R. van Leeuwen, Time propagation of the Kadanoff-Baym equations for inhomogeneous systems, J. Chem. Phys. 130 (2009) 224101.

[7] P. Danielewicz, Quantum theory of nonequilibrium processes, I, Annals of Physics 152 (2) (1984) 239–304.

[8] M. Bonitz, D. Kremp, D. Scott, R. Binder, W.-D. Kraeft, H. S. Köhler, Numerical analysis of non-Markovian effects in charge-carrier scattering: one-time versus two-time kinetic equations, Journal of Physics: Condensed Matter 8 (33) (1996) 6057.

[9] F. Hoppensteadt, Z. Jackiewicz, B. Zubik-Kowal, Numerical solution of Volterra integral and integro-differential equations with rapidly vanishing convolution kernels, BIT Numerical Mathematics 47 (2) (2007) 325–350.

[10] C. A. Kennedy, M. H. Carpenter, Diagonally Implicit Runge-Kutta methods for ordinary differential equations, a review, National Aeronautics and Space Administration, Langley Research Center, 2016.

[11] N. H. Kwong, M. Bonitz, R. Binder, H. Köhler, Semiconductor Kadanoff-Baym Equation Results for Optically Excited Electron–Hole Plasmas in Quantum Wells, physica status solidi (b) 206 (1) (1998) 197–203.

[12] N.-H. Kwong, M. Bonitz, Real-time Kadanoff-Baym approach to plasma oscillations in a correlated electron gas, Physical review letters 84 (8) (2000) 1768.

[13] N. Schlünzen, J.-P. Joost, M. Bonitz, Comment on "On the unphysical solutions of the Kadanoff-Baym equations in linear response: Correlation-induced homogeneous density-distribution and attractors", Phys. Rev. B 96 (11) (2017) 117101.

[14] N. Schlünzen, S. Hermanns, M. Scharnke, M. Bonitz, Ultrafast dynamics of strongly correlated fermions—nonequilibrium Green functions and selfenergy approximations, J. Phys. Condens. Matter 32 (10) (2019) 103001.

[15] M. P. Von Friesen, C. Verdozzi, C.-O. Almbladh, Successes and failures of Kadanoff-Baym dynamics in Hubbard nanoclusters, Physical review letters 103 (17) (2009) 176404.

[16] T. A. Burton, Volterra integral and differential equations, Vol. 202, Elsevier, 2005.

[17] P. J. Schmid, Dynamic mode decomposition of numerical and experimental data, J. Fluid Mech. 656 (2010) 5–28.

[18] P. J. Schmid, Application of the dynamic mode decomposition to experimental data, Exp. Fluids 50 (4) (2011) 1123–1130.

[19] P. J. Schmid, L. Li, M. P. Juniper, O. Pust, Applications of the dynamic mode decomposition, Theor. Comput. Fluid Dyn. 25 (1) (2011) 249–259.

[20] P. J. Schmid, D. Violato, F. Scarano, Decomposition of time-resolved tomographic PIV, Exp. Fluids 52 (6) (2012) 1567–1579.

[21] A. Seena, H. J. Sung, Dynamic mode decomposition of turbulent cavity flows for self-sustained oscillations, Int. J. Heat Fluid Flow 32 (6) (2011) 1098–1110.

[22] J. Grosek, J. N. Kutz, Dynamic mode decomposition for real-time background/foreground separation in video, arXiv preprint arXiv:1404.7592 (2014).

[23] J. N. Kutz, X. Fu, S. L. Brunton, N. B. Erichson, Multi-resolution dynamic mode decomposition for foreground/background separation and object tracking, in: 2015 IEEE International Conference on Computer Vision Workshop (ICCVW), IEEE, 2015, pp. 921–929.

[24] J. L. Proctor, P. A. Eckhoff, Discovering dynamic patterns from infectious disease data using dynamic mode decomposition, Int. Health 7 (2) (2015) 139–145.

[25] J. Yin, Y.-h. Chan, F. da Jornada, D. Qiu, C. Yang, S. G. Louie, Analyzing and predicting non-equilibrium many-body dynamics via dynamic mode decomposition, arXiv preprint arXiv:2107.09635 (2021).

[26] J. N. Kutz, S. L. Brunton, B. W. Brunton, J. L. Proctor, Dynamic mode decomposition: data-driven modeling of complex systems, SIAM, 2016.

[27] S. Le Clainche, J. M. Vega, Higher order dynamic mode decomposition, SIAM J. Appl. Dyn. Syst. 16 (2) (2017) 882–925.

[28] J. H. Tu, C. W. Rowley, D. M. Luchtenburg, S. L. Brunton, J. N. Kutz, On dynamic mode decomposition: Theory and applications, J. Comput. Dyn. 1 (2) (2014) 391–421.

[29] H. Arbabi, I. Mezić, Ergodic theory, dynamic mode decomposition, and computation of spectral properties of the Koopman operator, SIAM J. Appl. Dyn. Syst. 16 (4) (2017) 2096–2126.

[30] B. O. Koopman, Hamiltonian systems and transformation in Hilbert space, Proc. Natl. Acad. Sci. U.S.A. 17 (5) (1931) 315.

[31] B. O. Koopman, J. v. Neumann, Dynamical systems of continuous spectra, Proc. Natl. Acad. Sci. U.S.A. 18 (3) (1932) 255.

[32] G. H. Golub, C. F. Van Loan, Matrix computations, Vol. 3, JHU press, 2013.

[33] M. Williams, I. Kevrekidis, C. Rowley, A Data–Driven Approximation of the Koopman Operator: Extending Dynamic Mode Decomposition, J. Nonlinear Sci. 25 (2015) 1307–1346.

[34] D. S. Broomhead, G. P. King, Extracting qualitative dynamics from experimental data, Phys. D 20 (2-3) (1986) 217–236.

[35] N. H. Packard, J. P. Crutchfield, J. D. Farmer, R. S. Shaw, Geometry from a time series, Phys. Rev. Lett. 45 (9) (1980) 712–716.

[36] S. Pan, K. Duraisamy, On the structure of time-delay embedding in linear models of non-linear dynamical systems, Chaos 30 (7) (2020) 073135.

[37] F. Takens, Detecting strange attractors in turbulence, in: Dynamical systems and turbulence, Warwick 1980, Springer, 1981, pp. 366–381.

[38] J. Hubbard, Electron correlations in narrow energy bands, Proc. Math. Phys. Eng. Sci. P ROY SOC A-MATH PHY 276 (1365) (1963) 238–257.

[39] H. Tasaki, The Hubbard model-an introduction and selected rigorous results, Journal of Physics: Condensed Matter 10 (20) (1998) 4353.

[40] S. R. White, D. J. Scalapino, R. L. Sugar, E. Loh, J. E. Gubernatis, R. T. Scalettar, Numerical study of the two-dimensional Hubbard model, Phys. Rev. B 40 (1) (1989) 506.

[41] P. Lipavskỳ, V. Špička, B. Velickỳ, Generalized Kadanoff-Baym ansatz for deriving quantum transport equations, Phys. Rev. B 34 (10) (1986) 6933.

[42] S. Hermanns, K. Balzer, M. Bonitz, Non-equilibrium Green's function approach to inhomogeneous quantum many-body systems using the Generalized Kadanoff Baym Ansatz, Phys. Scr. 2012 (T151) (2012) 014035.

[43] N. Schlünzen, J.-P. Joost, M. Bonitz, Achieving the scaling limit for nonequilibrium green functions simulations, Phys. Rev. Lett. 124 (7) (2020) 076601.

Highlights

- Use Dynamic mode decomposition (DMD) and higher order DMD (HODMD) to approximate the two-time nonequilibrium Green's function
- Examine and compare several schemes for partitioning a two-time Green's function into several one-time funcitons
- Demonstrate the efficiency and accuracy of DMD and HODMD on a model two-band system
- Use band structure and spectral functions to validate the accuracy of DMD approximation

Jia Yin

Jia Yin is a postdoc in the Applied Mathematics and Computational Research Division at Lawrence Berkeley National Lab (LBNL). She got her Ph.D. from National University of Singapore in 2019, and was a Research Fellow there from 2019 to 2020. After that, she joined LBNL as a postdoc. Her major research interests lie in the numerical methods for highly oscillatory partial differential equations (PDEs), multiscale modeling and simulation, and quantum many-body problems.

Yang-hao Chan

Yang-hao Chan is an assistant Research Fellow in the Institute of Atomic and Molecular Sciences, Academia Sinica. Before he joined IAMS he was a Project Scientist at Lawrence Berkeley National Lab from 2017 to 2020. He got his PhD in physics from University of Michigan, Ann Arbor in 2013. He worked as a Postdoc researcher in IAMS from 2014 to 2017. His research interests include first-principles calculations of excited states, simulations of time-dependent phenomena, and quantum phases in the strongly correlated systems.

Felipe H. da Jornada

Felipe H. da Jornada is an Assistant Professor in Materials Science and Engineering at Stanford University. He received his Ph.D. from UC Berkeley in 2017 and was awarded the Kavli Nanoscience Institute at Berkeley Best Thesis Award. His research uses a combination of theory and algorithm development with high-performance computer calculations to predict the electronic and optical properties of novel materials without empirical fitting parameters (i.e., from first principles). Jornada is interested in the electronic properties of atomically thin, quasi-2D materials, and in utilizing excited-state calculations to address questions related to quantum materials and renewables.

Diana Y. Qiu

Diana Y. Qiu is an Assistant Professor of Mechanical Engineering and Materials Science at Yale University. She received her Ph.D. from UC Berkeley in 2017, after which she was a postdoctoral researcher at Lawrence Berkeley National Lab (LBNL). She joined Yale University in 2020, where her research is supported by a DOE Early Career award and a Packard Fellowship for Science and Engineering. Her research interests lie in developing and applying first principles theories to understand the excited state properties of novel materials, especially excitons in 2D materials.

Steven G. Louie

Steven G. Louie received his physics Ph.D. from University of California at Berkeley in 1976. After having worked at the IBM Watson Research Center, Bell Labs, and U of Penn, he joined the UC Berkeley faculty in 1980, where he is a distinguished professor of physics and a senior faculty scientist at the Lawrence Berkeley National Lab. He is an elected member of the National Academy of Sciences, Chinese Academy

of Sciences, American Academy of Arts & Sciences, and Academia Sinica, as well as fellow of the American Physical Society (APS), American Association for the Advancement of Science, and Materials Research Society (MRS). He is a recipient of the APS Rahman Prize, APS Davisson-Germer Prize, MRS Materials Theory Award, and Foresight Institute's Feynman Prize, among others. His research is in theoretical and computational condensed matter physics. Louie has published over 675 papers (Google Scholar h-index of 164 and total citations of over 118,000). He is known for his development of the ab initio GW method and for his studies of novel materials and reduced-dimensional systems.

Chao Yang

Chao Yang is a senior scientist in the Applied Mathematics and Computational Research Division at Lawrence Berkeley National Laboratory (LBNL). He received his Ph.D. from Rice University in 1998. He was a Householder fellow at the Oak Ridge National Laboratory from 1999 to 2000. He joined LBNL in 2000. His research interests include numerical linear algebra with applications in electronic structure calculations and quantum many-body problems, inverse problems, and high performance computing and machine learning. He is a member of SIAM.

Declaration of interests

☒ The authors declare that they have no known competing financial interests or personal relationships that could have appeared to influence the work reported in this paper.

☐The authors declare the following financial interests/personal relationships which may be considered as potential competing interests: